HEFT

D3.2 Improved SiC-based high voltage drive control

Funded by
the European Union

Call	HORIZON- CL5-2020-D5-01	
GA Number	101096306	
Deliverable No.	D3.2	
Deliverable Title	Improved SiC-based high voltage drive control	
Deliverable Date	2024-07-04	
Contractual delivery	2023-05-31	
Deliverable Type	R	
Dissemination level	PU	
Status	V2.0	2024-07-04

Written By	Maitane, Carrasco, Amaia López de Heredia, Ion Iturbe	2024-07-02
Checked by	Fernando Garramiola	2024-07-03
Approved by	Javier Poza	2024-07-04

HORIZON CL5-2020-D5-01. HEFT 101096306 – Novel concept of a Low Cost, High Power Density and Highly Efficient Recyclable motor for next generation mass produced electric vehicles

Acknowledgement:

The author(s) would like to thank the partners in the project for their valuable comments on previous drafts and for performing the review.

Project partners:

1. MGEP (Mondragon Goi Eskola Politeknikoa Jose Maria Arizmendiarrieta S Coop).
2. GKN (GKN Driveline Zumaia SA).
3. GKN AIC (GKN Automotive Innovation Center - GKN Hybrid Power Ltd.).
4. MAGNETI (Magneti Ljubljana d.d.).
5. VYNCOLIT (Vyncolit N.V.).
6. IKERLAN (IKERLAN S. Coop.).
7. UNIBO (Alma Mater Studiorum - Università di Bologna).
8. KUL (Katholieke Universiteit Leuven).
9. UoN (University of Nottingham).

TABLE OF CONTENTS

GLOSSARY

Abbreviation/ acronym	Description
AC	Alternative Current
DC	Direct Current
EU	European Union
FW	Flux Weakening
GBD	Grain Boundary Diffusion
IPMSM	Interior Permanent Magnet Synchronous Motor
LUT	Look-up-Table
MTPA	Maximum Torque per Ampere
MTPV	Maximum Torque per Voltage
PI	Proportional Integral
PWM	Pulse Width Modulation
SiC	Silicon Carbide
VC	Vector Control
WP	Work Package

1 EXECUTIVE SUMMARY

Climate change has created an increased need for innovation in various sectors, including the automotive industry. Many corporations are striving to fulfil this need by developing and producing electric cars. However, the production process remains inefficient and environmentally harmful. The EU-funded HEFT project will reverse this trend by introducing a revolutionary synchronous motor for electric cars, which will be recyclable, cost-efficient and require fewer materials while producing fewer emissions and creating novel European circular economies.

HEFT Project proposes a set of innovation challenges on electric synchronous motor configuration based on SiC inverters (direct cooling of rotor and stator, advance insulation for high voltage, multibarrier rotor topology, wave windings) and advanced materials (advanced GBD magnets, epoxy for magnet fixation, composite for motor housing, insulation resin). These innovations will result in a high-efficient and low-cost solution that will be validated on 2 motor topologies.

- Motor topology type C: Motors for C-D-E vehicle segments.
- Motor topology type A: Motors for A-B vehicle segments.

In this document the work carried out in Task 3.2 of HEFT project has been summarized. The objective of this task is to improve SiC-based drive control to reduce powertrain losses and improve EV range. In this document the following issues will be covered:

1. Online variable switching frequency control strategy to optimize drive operation and reduce inverter and motor losses.
2. Optimal flux operation point to increase motor efficiency.
3. Improved powertrain thermal management strategy.

All these control aspects will be used in both A+B segment motor and C+D+E segment motor, as control strategy is the same for both motors that will be designed in HEFT project (only some parameters' tunning need to be modified). Therefore, as use case, A+B segment motor has been selected, because this motor has already been designed. However, some preliminary results regarding C+D+E segment motor are also shown in this deliverable (this motor is still under development) to show that the proposed control strategy is valid for any IPMSM.

2 DRIVE SPECIFICATIONS AND MOTOR PARAMETERS

In this section, drive specifications considered for this task will be described. These specifications were defined in WP1 (Deliverable D1.2). On the one hand, there are two segments of vehicles considered (A+B and C+D+E), leading to two different motors. On the other hand, silicon carbide (SiC) inverter will be detailed. Two different motors specifications are detailed in Table 1 and Table 2.

Table 1 Motor Specifications for A+B segment.

A + B Segment			
	Units	**Peak**	**Continuous**
Duration of operation point	S	30	1800
Shaft power	kW	110	55
Max Shaft torque - example	Nm	163	
Corner speed	rpm	6.444	
Maximum speed - example	rpm	20.000	
Maximum speed - market constraint	rpm	20.000	
Maximum overspeed	rpm	+10%	
Nominal DC Voltage	Vdc	650	
Maximum phase current	Arms	350	
Power Density - Continuous		~27,7kW/L (KPI3.2) & ~8,39kW/kg (KPI 4.1)	
Torque Density - Continuous		~55,87 Nm/L & ~35,84Nm/kg (KPI 4.2)	
Motor losses - Mean over WLTP	Wh/km		11,4
Maximum temperature on winding	°C	180	180
Maximum rotor temperature	°C	150	150

Table 2 Motor specifications for C+D+E Segment

C + D + E Segment			
	Units	**Peak**	**Continuous**
Duration of operation point	S	30	1800
Shaft power	kW	170	111
Max Shaft torque - example	Nm	260	
Corner speed	rpm	6.250	
Maximum speed - example	rpm	19.914	
Maximum speed - market constraint	rpm	20.000	
Maximum overspeed	rpm	+10%	
Nominal DC Voltage	Vdc	650	
Maximum phase current	Arms	350	
Power Density - Continuous - Option A		~28,1kW/L (KPI3.2) & ~7,07kW/kg (KPI 4.1)	
Torque Density - Continuous - Option B		~50,18 Nm/L & ~32,19Nm/kg (KPI 4.2)	
Motor losses - Mean over WLTP	Wh/km		TBD[1]
Maximum temperature on winding	°C	180	180
Maximum rotor temperature	°C	150	150

SiC inverter specifications are described in Table 3.

Table 3 SiC inverter specifications

SiC inverter			
dV/dt & Risetime (maxDCBus / (dU/dt) = risetime)	[kV/µs]	5 typical	10 stretch
Max Switching Frequency	[Hz]	20.000	
Fundamental Frequency max	[Hz]	~1000	
Number of phases	[-]	3	
max. DC-Bus-Voltage	Vdc	800	
PDIV Phase-Phase	Vpk-pk	3726	
PDIV Phase-Ground	Vpk-pk	2381	

Moreover, to tune control strategy algorithm is necessary to consider motor design parameters. A+B segment motor have already been defined in WP4 (Task 4.1) and the following design parameters have been selected:

Table 4 A+B segment motor design parameters (at maximum saturation levels).

A+B HEFT motor		
Pole pair	[-]	3
L_d	[mH]	0.155
L_q	[mH]	0.4293
R_s	[mΩ]	27.37
Magnet flux (RMS)	[mWb]	48.3

[1] Motor losses - Mean over WLTP. To Be Defined according to fulfil at least 20% reduction over baseline eMotor

3 IMPROVED SIC-BASED IPMSM DRIVE CONTROL STRATEGY

In this section the control strategy developed for an 800V SiC based drive is presented. Firstly, main control parts of the vector control will be described. Then, improved control algorithms will be introduced: variable switching frequency, optimal flux operation point, and thermal derating.

3.1 IPMSM Drive control

The Vector Control (VC) is implemented for the control of the IPMSM SiC-based drive control. This control algorithm decomposes the AC current vector into two perpendicular DC components. These components are named as direct current (id) and quadrature currents (iq). The former is oriented as the axis of the permanent magnet of the rotor. The latter leads $90°$ to the q-axis. In Figure 1 this transformation is shown graphically, where *x* represents any electrical variable such as voltage or current and θ_e the electrical angular position.

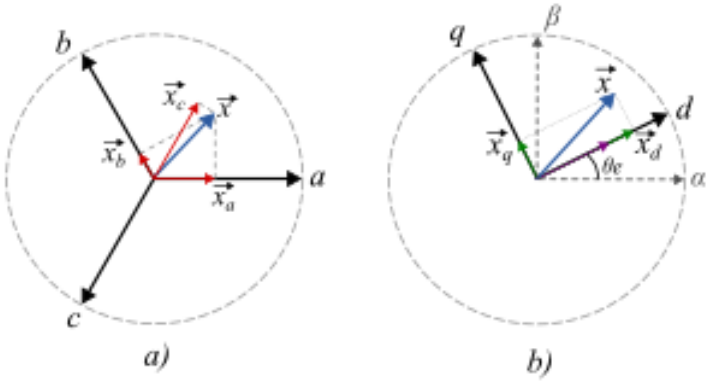

Figure 1: abc to dq transformation.

In synchronous machines, two constraints exist which are imposed by the inverter and the machine. These limits impose the current references for the control of the drive. On the one hand, the current limitation comes from the thermal limitation in the inverter and the machine. This limitation is defined in (1). On the other hand, the voltage limit defined by (2) is imposed by the isolation of the machine and the maximum voltage that can be supplied by the inverter.

$$i_{ds}^2 + i_{qs}^2 \leq I_s^2 \quad (1)$$

$$v_{ds}^2 + v_{qs}^2 \leq V_s^2 \quad (2)$$

Until a certain speed of the machine, known as base speed, the voltage limitation is not a constraint since the maximum voltage is not reached. This region is called the constant torque region. After the base speed is reached, the phase voltage amplitude is maintained constant, and the torque maximum value is indirectly proportional to the fundamental speed of the machine. This region is the flux-weakening region [1].

To obtain the current references in the constant torque region Maximum Torque Per Ampere (MTPA) is selected. This algorithm aims to calculate the most efficient idq current reference value for a torque contour. In Figure 2 the combination of idq currents for each torque contour are shown for HEFT A+B segment motor. The MTPA trajectory shows the most efficient combination of idq currents for each torque value.

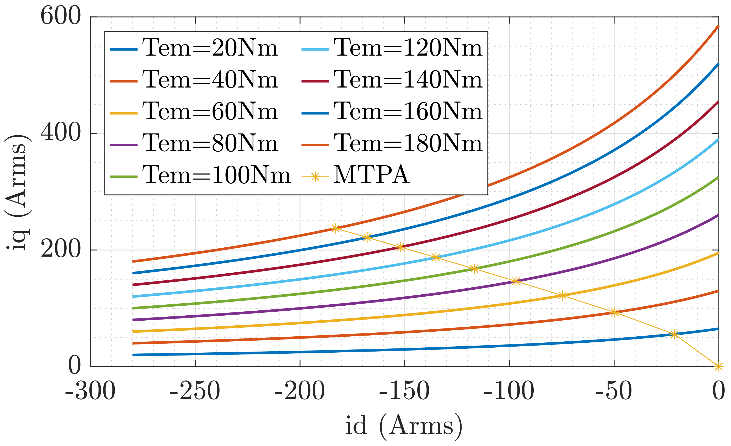

Figure 2: Torque contours vs idq currents for MTPA algorithm.

The direct and quadrature currents can be expressed as a function of the stator maximum value as shown in (3). In this way, the resultant torque equation given by (4). The current angle that achieves the maximum torque for an idq current combination is obtained by deriving the torque equation (4) by the angle of the current as $dT_{em}/d\delta$. Thus, the optimum current angle is calculated by (5). For this drive, the resultant idq trajectory respect to the torque value is shown in Figure 3.

$$i_{ds} = -I_s \sin\delta \tag{3}$$

$$i_{qs} = I_s \cos\delta$$

$$T_{em} = \frac{3}{2} p\left(\lambda_{pm} I_s \cos\delta + (L_{ds} - L_{qs}) I_s^2 cos\delta sin\delta\right) \tag{4}$$

$$\sin\delta_{MTPA} = \frac{\lambda_{pm}}{2(L_q - L_d)} - \sqrt{\frac{\lambda_{pm}^2}{4(L_q - L_d)^2} + I_s^2} \tag{5}$$

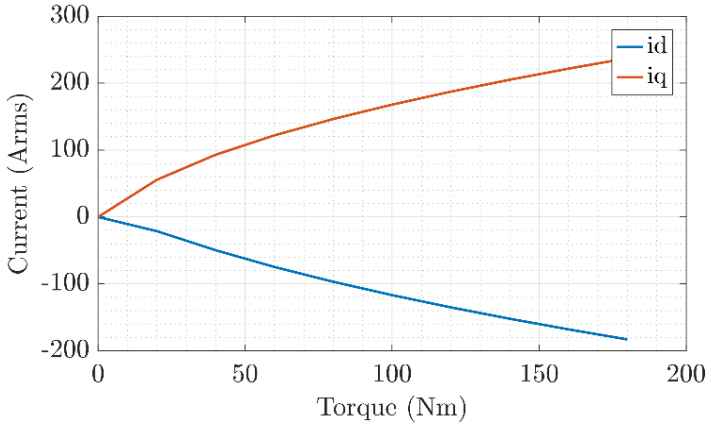

Figure 3: Tem vs idq for MTPA algorithm for HEFT A+B segment motor.

As mentioned previously, in the flux-weakening (FW) region the voltage is also a constraint. In this case, the optimum current angle is achieved by resolving the voltage equation shown in (6). The resultant current angle is calculated by (7).

$$V_{max} = \omega_e \sqrt{\left(-L_q I_s \cos\delta\right)^2 + \left(L_d I_s \sin\delta + \lambda_{pm}\right)^2} \tag{6}$$

$$\sin \delta_{FW} = \frac{-L_d \lambda_{pm} + \sqrt{L_q^2 \lambda_{pm}^2 + (L_q^2 - L_d^2)(L_q^2 I_s^2 - V_{max}^2/\omega_e^2)}}{(L_q^2 - L_d^2) I_s} \quad (7)$$

Finally, in some drives, an additional third region called Maximum Torque per Voltage (MTPV) can be implemented. This region happens in drives that fulfil the relation $\lambda_{pm} < L_{ds} I_s$, which places the centre of the voltage ellipse inside the current circumference. In this case, this condition is not given, thus, the MTPV is not applied. In Figure 4 it is verified how the MTPV trajectory does not enter the circumference of the current at the maximum machine speed for Vdc=650V.

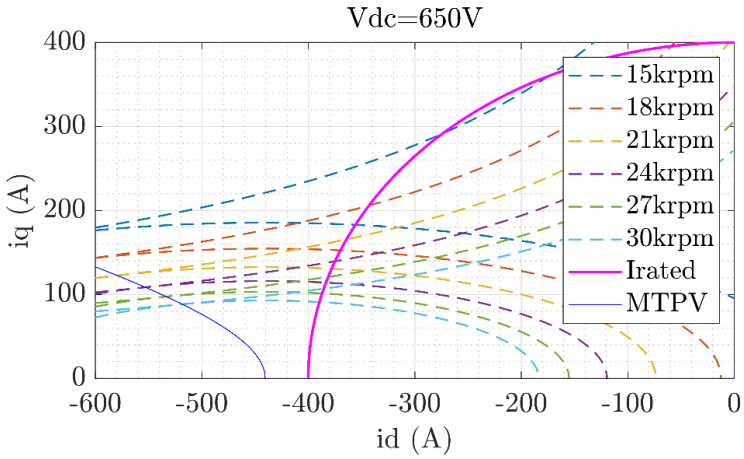

Figure 4: MTPV trajectory for the considered drive.

After calculating the idq references for the full-speed region, the characteristics curves of the drive are shown in Figure 5. In this case, the base speed is $N_{base} = 20.000$rpm.

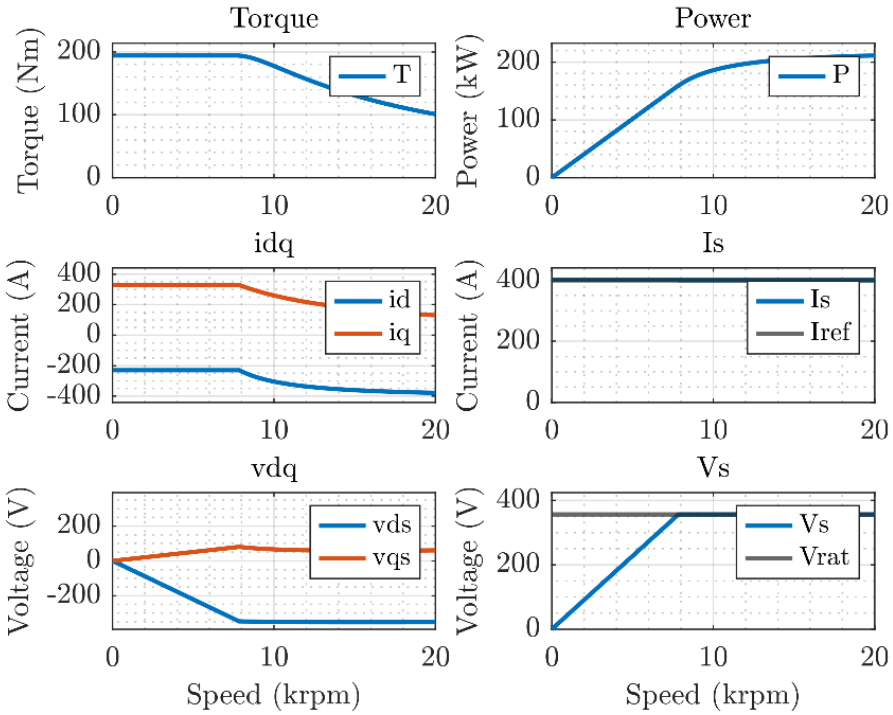

Figure 5: Characteristics curves of the IPMSM for HEFT A+B segment motor.

For the implementation of the explained algorithms, the block diagram shown in Figure 6 is followed. First, the idq current references for the commanded torque reference T_{em}* are obtained from the Look-Up-Table (LUT) *MTPA & FW*. The vdq reference voltages are obtained from the

current regulators which in this control are Proportional-Integral (PI) regulators. The inputs for these regulators are the idq^* and the measured $idq\ fb$ currents. The latter are obtained from the information given by the current sensor. These phase currents are transformed to dq coordinates through the abc to $dq0$ transformation, see equation (8).

$$\begin{bmatrix} f_d \\ f_q \\ f_0 \end{bmatrix} = \frac{2}{3} \begin{bmatrix} \cos\theta & \cos(\theta - 2\pi/3) & \cos(\theta + 2\pi/3) \\ -\sin\theta & -\sin(\theta - 2\pi/3) & -\sin(\theta + 2\pi/3) \\ 1/2 & 1/2 & 1/2 \end{bmatrix} \begin{bmatrix} f_a \\ f_b \\ f_c \end{bmatrix} \quad (8)$$

Once the vdq reference voltages are calculated, the inverse of the abc to $dq0$ transformation is applied to achieve the voltage reference in *abc* frame. Finally, the voltage reference obtained from the control is fed to the modulation block. The implemented modulation in this block in the third harmonic injection which increases the index modulation to $ma = 1.15$. To obtain the gate pulses required from the semiconductors, the PWM modulation is selected where a high switching frequency triangular carrier is compared with the voltage reference commands obtained from the control.

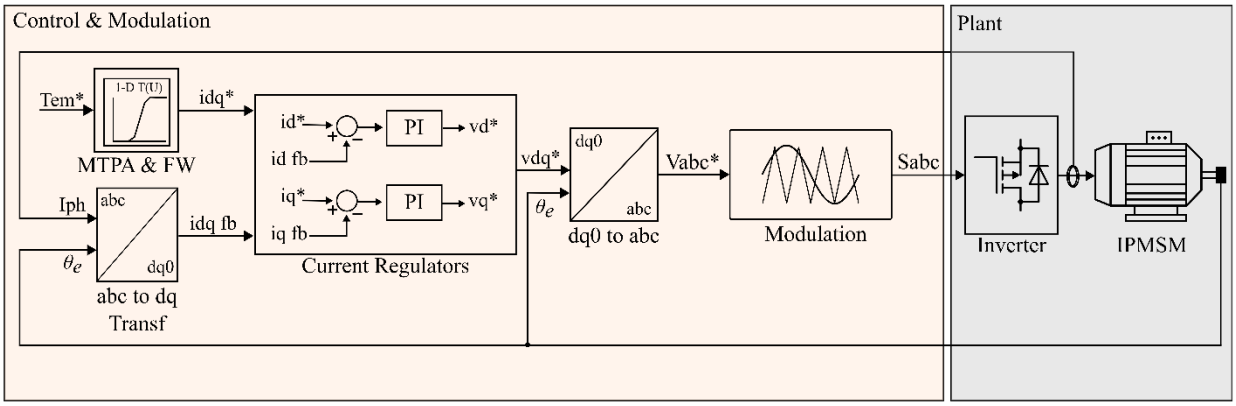

Figure 6: Control block diagram of the IPMSM SiC-based drive.

3.2 Variable switching frequency control to reduce losses

One of the advantages of SiC devices is their wide range of switching frequencies. To take advantage of this characteristic and at the same time improve the efficiency of the SiC-based inverter drive, a variable switching frequency control is implemented. Different objectives are presented in the literature for the variable switching frequency control as shown in [2], [3], and [4].

In this case, the selected objective of the variable switching frequency control is to maintain a frequency ratio $m_f = 17$. Following this criterion, the switching frequency varies depending on the speed of the machine as shown in Figure 7. A minimum switching frequency of $f_{sw} = 5$kHz is fixed at low speeds to ensure good control accuracy in this region.

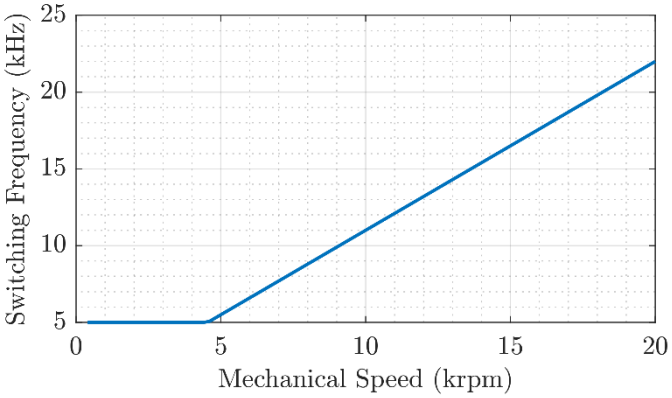

Figure 7: Mechanical Speed vs Switching frequency ratio for m_f=17.

3.3 Optimal flux operation point to increase motor efficiency

In section 3.1, the fundamentals of the control of an IPMSM have been explained, including the operational limits related both to the machine and to the inverter. Related to that explanation Figure 8 shows the capacity curve of the machine. At lower velocities (less than 9500rpm), the torque limit is related to the current limit related to thermal limit. At higher velocities (more than 9500rpm) the torque limit is related to the voltage limit, that comes both from insulation voltage limit and operational maximum voltage related to the supply.

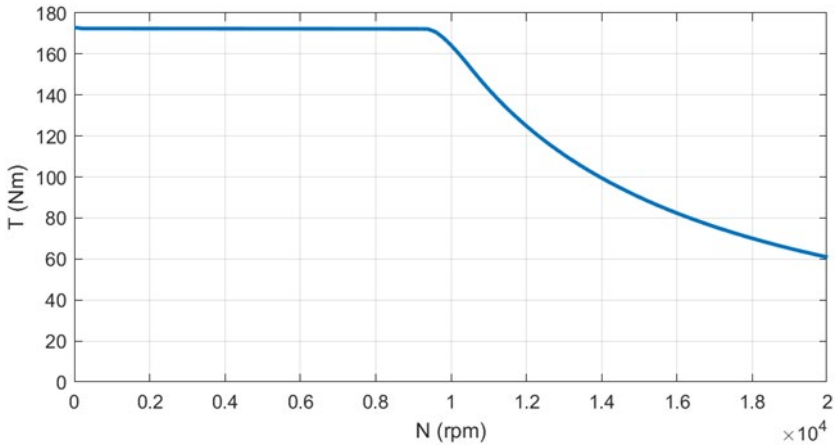

Figure 8:Torque-speed capacity of the machine.

The capacity curve is slightly influenced by the control strategy, but this section does not focus on pushing that limit but on selecting the optimum flux or the optimum d-q current setpoints for any point inside the capacity region. For example, which are the best dq current setpoints to operate the machine at N = 10 krpm and T = 80Nm? To answer this question, model of the machine, and the optimality criteria must be first analyzed.

3.3.1 Steady-state models of a IPMSM machines and optimal efficiency

The steady-state electrical model of a IPMSM machine can be written in function of currents and fluxes:

$$v_d = \mathrm{Rs} i_d - \omega_e \psi_q \qquad (9)$$

$$v_q = \mathrm{Rs} i_q + \omega_e \psi_d$$

where:

$$\psi_d = \psi_{\mathrm{pm}} + L_d i_d \qquad (10)$$

$$\psi_q = L_q i_q$$

And the torque equation is:

$$T = 3/2p\left(\psi_p m i_q + \left(L_d - L_q\right) i_d i_q\right) \qquad (11)$$

For vectors in complex coordinates $V_{dq} = v_d + j \cdot v_q$, $I_{dq} = i_d + j \cdot i_q$, $\psi_{dq} = \psi_d + j \cdot \psi_q$ the equivalent electric circuit of the IPMSM machine gets the shape shown in Figure 9:

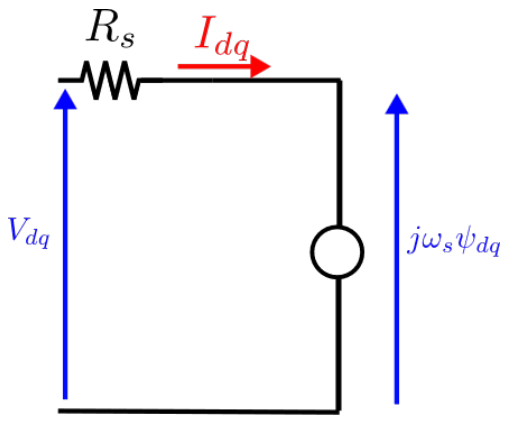

Figure 9. Fundamental electrical equivalent circuit of an IPMSM

In this model, the losses are Joule losses related to the power dissipated in the input resistance, and are then proportional to the square of the magnitude of the current:

$$P_{(R_s)} = R_s\left(i_d^2 + i_q^2\right) = R_s I_s^2 \tag{12}$$

The efficiency of the machine for a given output torque and speed is then:

$$e = \frac{T\omega_m}{T\omega_m + R_s I_s^2} \tag{13}$$

And to maximize it, the magnitude of the current must be minimized. This leads to the Maximum Torque Per Ampere (MTPA) optimization criteria, because getting the minimum current for a required torque comes to the same problem as getting the maximum torque for a given current magnitude.

3.3.2 IPMSM model including core losses

More advanced models, which also include losses related to magnetic field in different parts of the motor can be considered: usually, Finite Element Analysis software's provide information about the following type of losses:

- Hysteresis losses in iron.
- Eddy current losses in iron.
- Eddy current losses in magnets.

All these losses are localized at different parts of the machine and depend on the magnetic field and the frequency at each point of the machine. At each spatial point of the machine, the losses increase both with the amplitude of the magnetic field and with the frequency, with exponents and gains that depend on the properties of the material at each place. Several models such as Bertotti or Steinmetz [(MIT, s.f.)] can be used to model losses in different materials.

If a machine is analyzed as a system, the total losses are the addition of the losses at all the parts of the machine and depend on the magnetic state (so on dq currents) and on the frequency (so on the speed): if the rotating magnetic field is bigger, the losses are bigger, and if the speed is bigger the losses are bigger.

In an electrical equivalent circuit, such losses can be modeled by a resistor R_{nu} placed in parallel with the voltage source related to flux changes (Figure 10). And its value depends on the operating point (id, iq and speed/frequency).

$$R_{nu}\left(i_d, i_q, f\right) \tag{14}$$

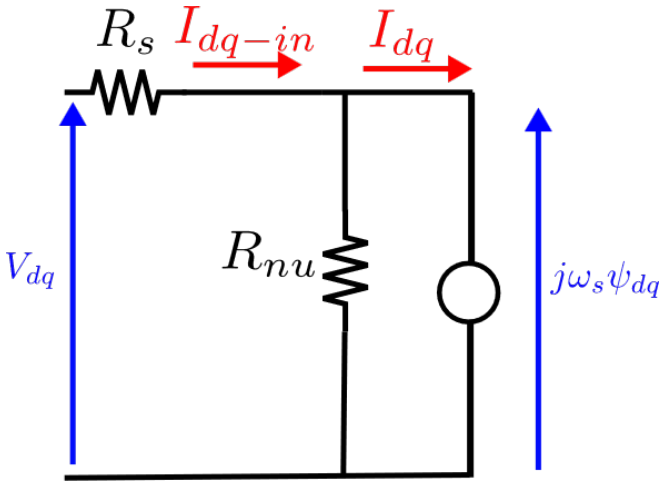

Figure 10: Electrical equivalent circuit of an IPMSM, including core losses.

In this new model, in addition to copper losses in R_s, there are also losses in R_{nu}, core losses, that depend on id, iq and velocity:

- At low velocities, core losses are small, and the most efficient point is almost MTPA point.
- When the speed increases, core losses can get not negligible, and the MTPA point is not the most efficient point.

The efficiency now contains also these core losses:

$$e = \frac{T\omega_m}{T\omega_m + R_s I^2_{(s-in)} + P_{nu}} \tag{15}$$

Figure 11 shows the behaviour of the losses, in such conditions, around the MTPA angle:

- Joule losses (blue line) have a minimum at the MTPA angle value. Changing the angle in any direction from this point will increase Joule losses.
- But for bigger angles, magnetic flux gets smaller so do the core losses (red line).
- So, the optimal, minimum losses point in total losses (orange line) is slightly displaced to a bigger angle than the MTPA angle.

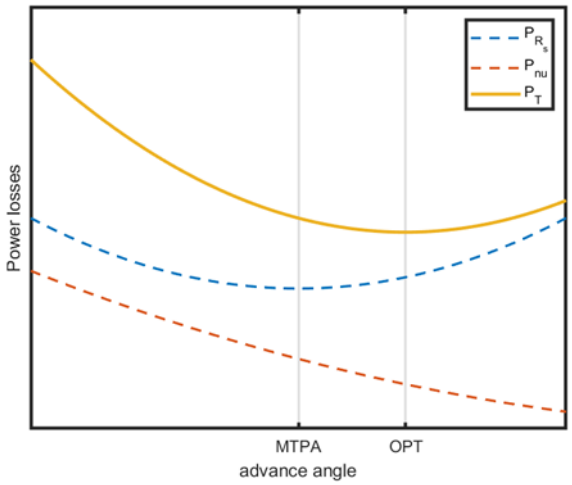

Figure 11: Power losses versus current advance angle, when considering core losses.

3.3.3 *Finding optimum fluxes and dq currents*

Finding the optimum operation point for each torque and speed gets a quite different approach depending on the complexity of the model of the machine.

- If a model with constant permanent magnet flux and constant inductances is considered (section 3.3.1), an analytical solution can be easily obtained.
- If a more detailed model that considers magnetic saturation is used, permanent magnet flux and inductances depend on dq currents, and the analytical solution gets impossible. Non-linear optimization techniques must then be used to find the MTPA solution. The solution is the same for all velocities.
- In case a model with saturation and with core losses is considered (shown in section 3.3.3.2), similar non-linear optimization techniques than in the previous are used, but the optimization criteria change to include core losses, and the optimum point depends on velocity.

3.3.3.1 MTPA with non-saturated model

The simplest model that can be considered for a IPMSM is a model with equations (9) and (10), in which the inductances L_d and L_q, and permanent magnet flux linkage ψ_{pm} are constant. Being constant meaning those values do not depend on currents.

With such model, an analytical calculation of the MTPA angle is possible. The calculation follows the following steps:

- First, dq currents are written depending on magnitude and advance angle .

$$i_{ds} = -I_s \sin\delta \qquad (16)$$
$$i_{qs} = I_s \cos\delta$$

- Second, those dq currents are replaced in equation (10), to get a torque equation that depends on current magnitude and angle:

$$T = \frac{3}{2} p\left[\psi_{pm} I_s \cos\delta - \left(L_d - L_q\right) I_s \sin\delta \, I_s \cos\delta\right] \qquad (17)$$

- To find the maximum torque for a given current Is value, the torque equation is derived to angle and equated to zero. Then, the angle is solved from that equation.

$$\sin\delta = \frac{\psi_{pm} - \sqrt{\psi_{pm}^2 + 8 I_s^2 \left(L_d - L_q\right)^2}}{4 I_s \left(L_d - L_q\right)} \qquad (18)$$

For example, for constant model parameters $L_d = 0.288mHr$, $L_q = 0.923mHr$ and $\psi_{pm} = 62.8mWb$, the torque-vs-angle curve of Figure 12 would be obtained for a constant current magnitude . The angle of the local maximum is at 33,5 degrees and can be calculated using equation (17).

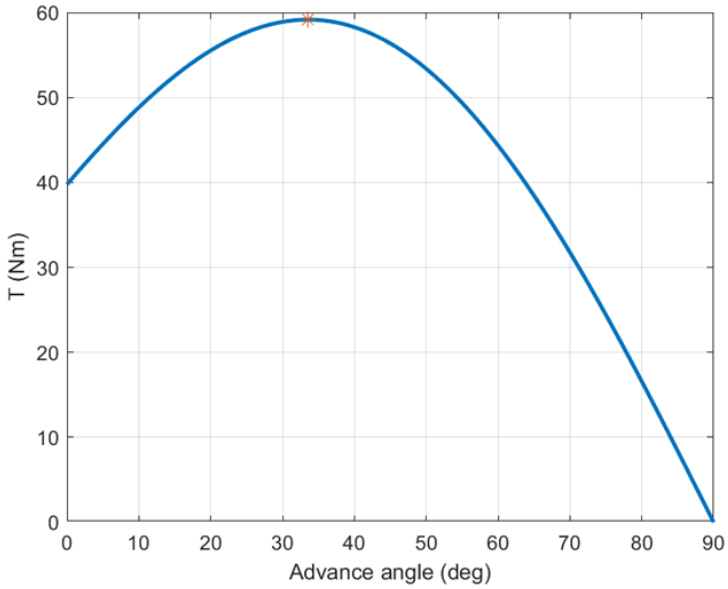

Figure 12: Torque vs advance angle, for a model with constant parameters.

3.3.3.2 MTPA with saturation-model

Using FEA analysis, motor models that consider magnetic saturation can be obtained. In such models equations (9) and (10) apply, but fluxes and inductances are values that change with dq currents: $L_d(i_d, i_q)$, $L_q(i_d, i_q)$ and , $\psi_{pm}(i_d, i_q)$.

Under such dependencies, it is not possible to find an analytical solution for the MPTA angle, and for each required torque, the point of minimum current must be found. For example, if current is applied at different advance angles, and the current required in each case to get 55Nm torque is plotted, the following result is obtained. The MTPA angle can be identified to be 43 degrees in this case (see Figure 13).

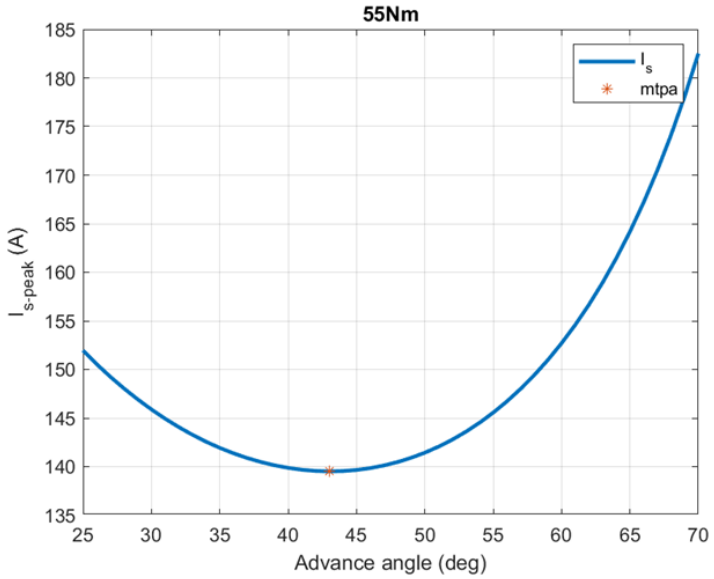

Figure 13: Current required to get 55Nm of torque, for AB model, depending on advance angle.

3.3.3.3 Optimum angle with saturation-model and core losses

As previously explained, when core losses are considered in the model, the total losses not only depend on dq currents, but also on velocity through core losses. The bigger the velocity, the bigger core losses, so looking for the optimum current angle at big speeds must consider those losses.

For example, stator copper losses, core losses and total losses are shown in Figure 14, for 20000rpm-55Nm operation point. Stator copper losses (blue line) have a local minimum at MTPA point, but core losses have a decreasing shape over the angle. Due to that, it happens that the local minimum of the total losses (opt) is displaced to the right side, to a slightly bigger angle.

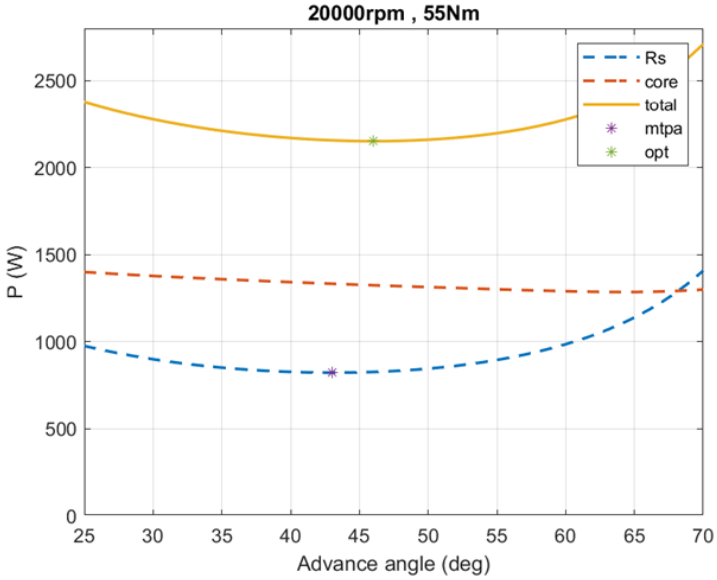

Figure 14: Power losses versus current advance angle, AB model, for 20000rpm and 55Nm

For lower velocities (Figure 14), core losses are smaller, while copper losses stay similar. As the speed decreases, the importance of core losses decreases, and the optimal efficiency operating point (opt) gets closer to the MTPA point. In Figure 14, at 2000rpm both points seem to be at the same angular position. In fact, as previously explained, for 0rpm, core losses would disappear and MTPA point would be equal to the optimum efficiency point.

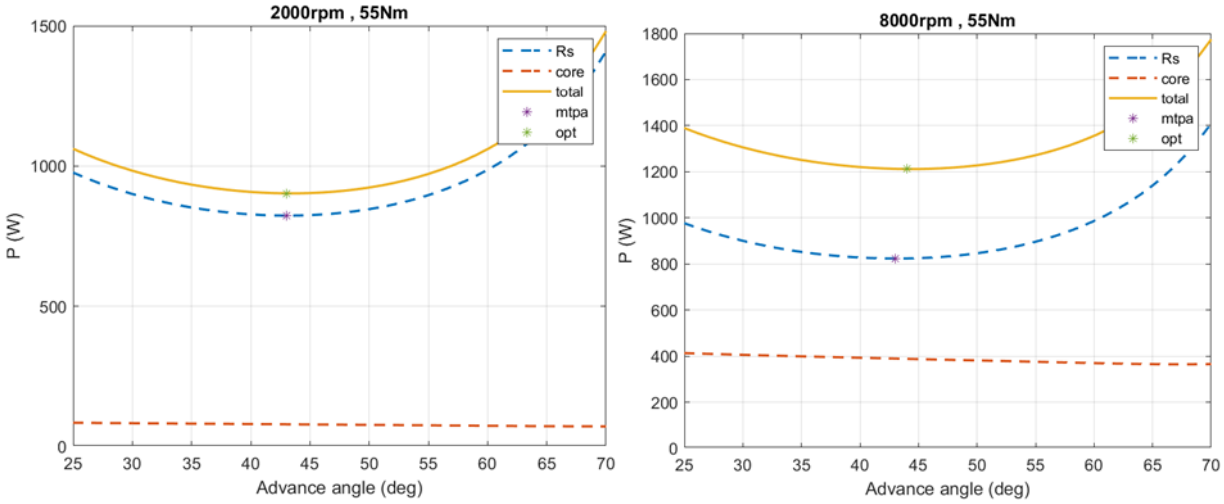

Figure 14: Power losses versus current advance angle, AB model, for 2000rpm and 8000rpm, and 55Nm

Thus, this last algorithm allows to operate at optimal flux operation to improve powertrain efficiency.

3.4 Improved powertrain thermal management strategy

To reduce the thermal stress of the drive, a thermal management strategy control can be implemented. The aim of this control algorithm is to reduce the current amplitude if a temperature threshold is reached. In this way, the thermal stress is reduced. To do this, the derating factor shown in Figure 15 is applied. In this case, the selected temperature threshold is $120℃$. Once this temperature value is achieved by the drive, the derating factor is applied to the i_{dq} currents.

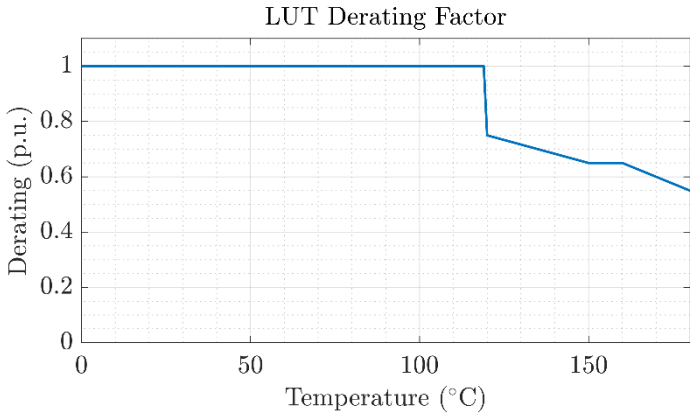

Figure 15: LUT of the derating factor for the improved powertrain thermal management strategy.

4 SIMULATIONS RESULTS: A+B SEGMENT MOTOR USE CASE

In this section the simulation results of the improved Control Strategy developed for the HEFT A+B segment motor are shown.

4.1 Basic performances

The basic performances of the drive are analysed in this section considering a constant switching frequency and a nominal flux operation. Moreover, no derating is applied if the drive is overheated. Maximum torque-speed characteristic results are shown.

In Figure 16 and Figure 17 the applied speed profile and the maximum torque profile are shown, respectively. The MTPA algorithm is applied in the constant torque region which ends at $N_{mec} = 7723.21$rpm. After this speed is reached, the flux weakening region is reached. In this region, the iq current amplitude must be indirectly proportional to the fundamental speed of the machine whereas the id current is directly proportional to the speed. Hence, the torque amplitude in this region decreases as the speed of the machine increases. At the maximum speed of the machine $N_{mec} = 20$krpm, the machine delivers a torque of $T_{em} = 100.82$Nm.

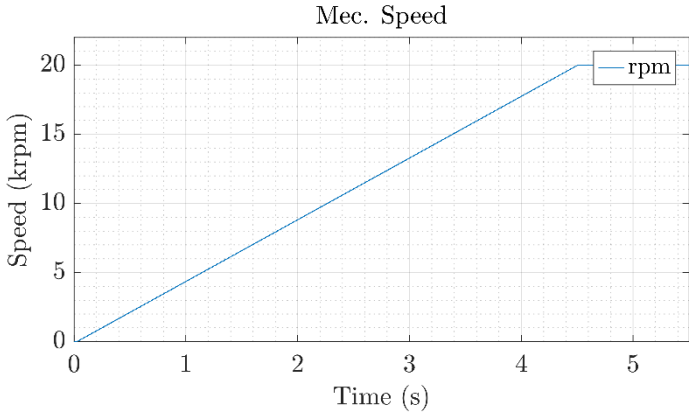

Figure 16: Speed profile applied to the analysed SiC drive.

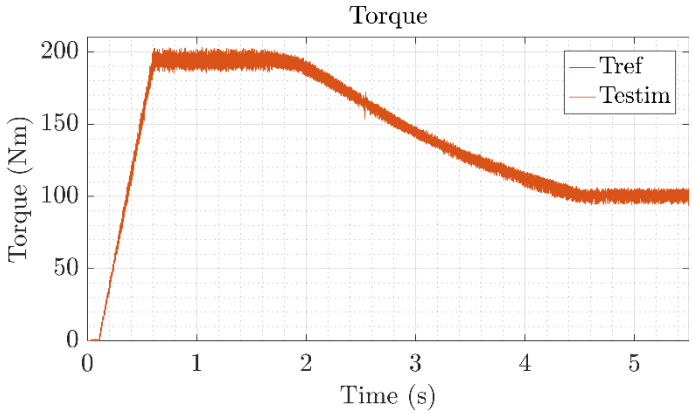

Figure 17: Simulation results of the reference (blue) and estimated torque (red).

The idq current references provided by the *MTPA & FW LUT* block and the feedback references of these signals are shown in Figure 18. As soon as the flux-weakening region is reached, iq current is decreased whereas the id current is increased. The id current is always negative to be able to deflux the machine. In Figure 19, the v*dq* voltage references are shown. These voltages are the output of the PI current regulators.

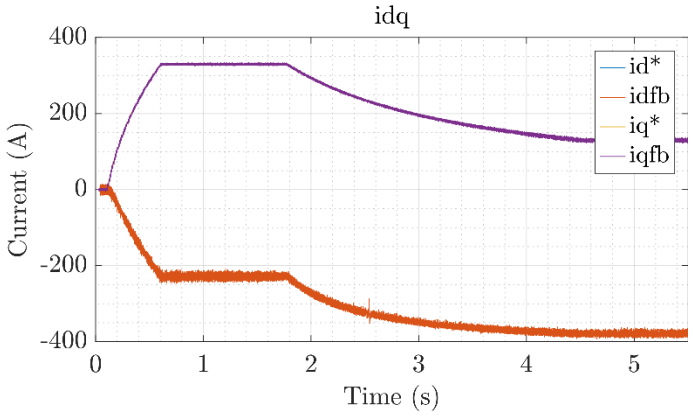

Figure 18: Simulation results of the reference and measured idq currents.

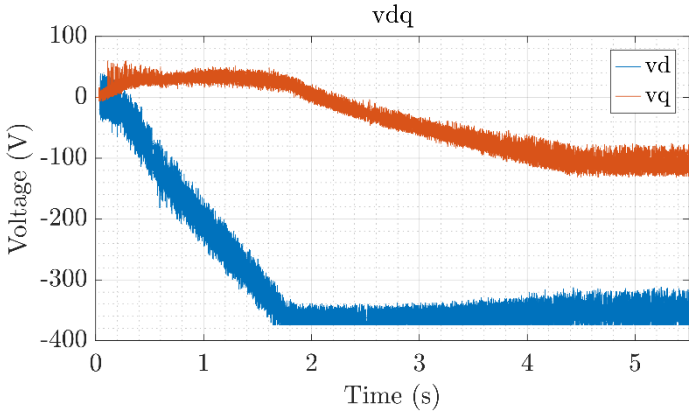

Figure 19: Simulation results of the resultant vdq voltage references.

The resultant voltage amplitude of the stator is shown in Figure 20. The maximum voltage of the stator $V_{s\,rat}$ is achieved at $N_{mec} = 7723.21$rpm. This speed matches the speed of the switching from constant torque to flux-weakening region.

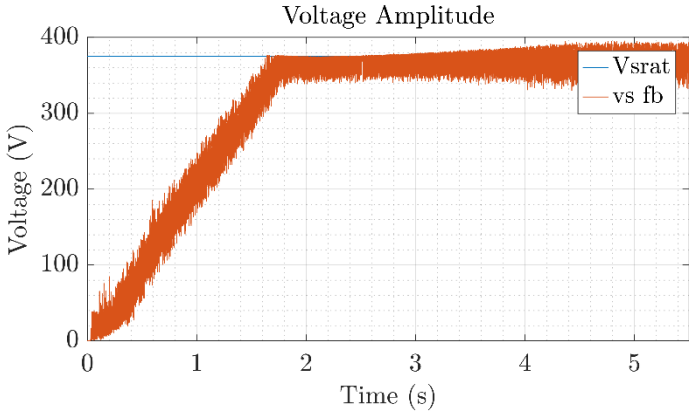

Figure 20: Simulation results of the voltage amplitude of the stator vs.

The estimated flux of the stator in *dq* frame are shown in Figure 21. As for dq current and torque values, the shift from the constant torque region to the flux-weakening region is done at $N_{mec} = 7723.21$rpm. It can be seen how λ_d flux increases its amplitude to demagnetize the machine.

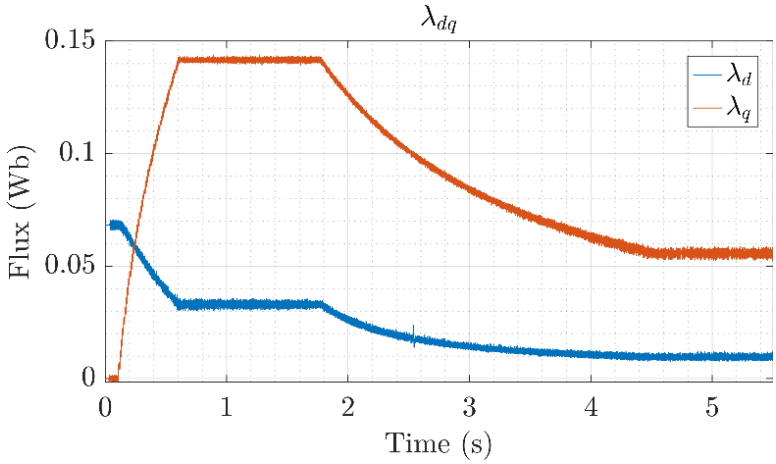

Figure 21: Simulation results of dq flux.

In Figure 22, the amplitude of the stator flux is shown. This amplitude achieves a maximum value of 145.81Wb in the constant torque region and a minimum value of 57.37Wb at maximum speed.

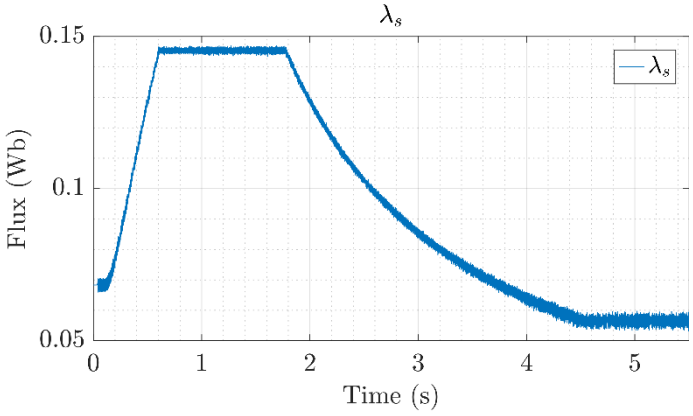

Figure 22: Simulation results of the amplitude of the stator flux.

The phase current in the constant torque and flux-weakening regions has a constant amplitude as shown in the Characteristics curves. In Figure 23 the resultant amplitude of the stator $I_s = 400.7$A is maintained in the full speed range. A zoom in the phase currents at the maximum speed $N_{mec} = 20000$rpm is shown in Figure 24. At this speed the resultant Total Harmonic Distortion is $THD_i = 2.50\%$.

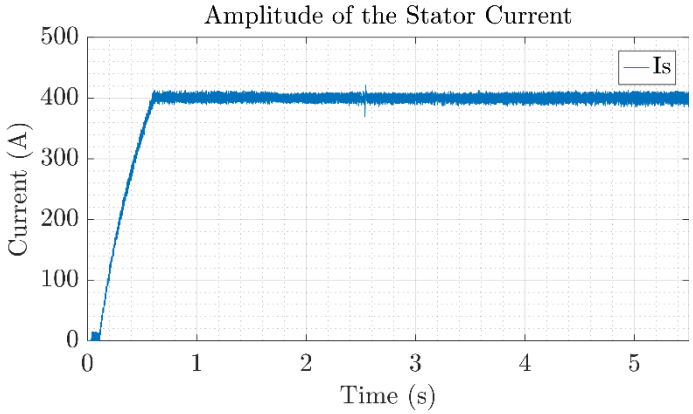

Figure 23: Simulation results of the phase currents.

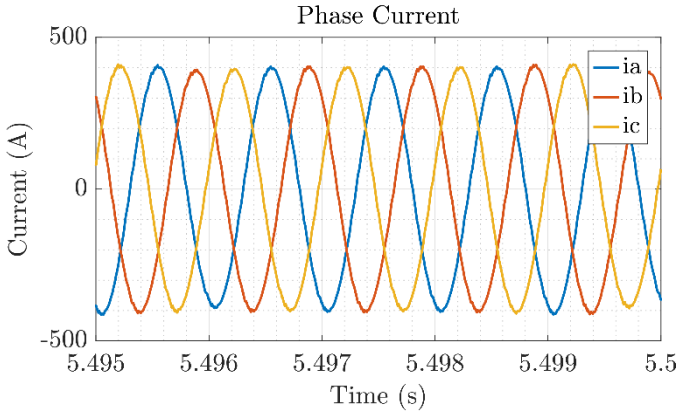

Figure 24: Zoom of the phase currents at N_{mec} = 20000 rpm.

Finally, a zoom of the duty cycles are shown in Figure 25. The maximum duty cycle value 1 p.u. is achieved at N_{mec} = 7723.21rpm, matching the region switching. The applied modulation adds the zero-sequence harmonic. For a three-phase a machine the zero-sequence harmonic corresponds to the 3^{rd} low-order harmonic. The amplitude of the added harmonic is $1/6$ of the amplitude of the injected harmonic. The implementation of this modulation is shown in Figure 26.

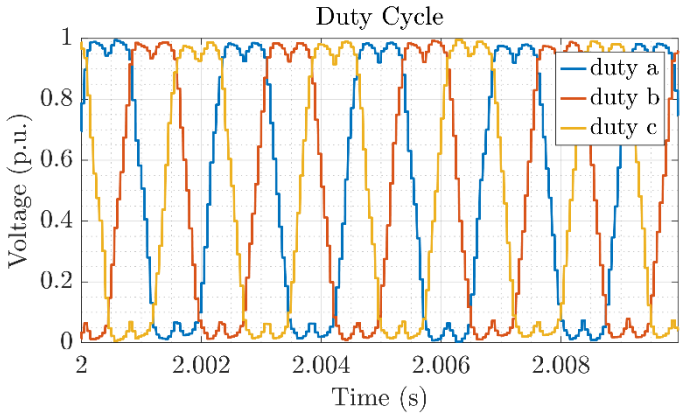

Figure 25: Zoom of the duty cycles in the constant torque region.

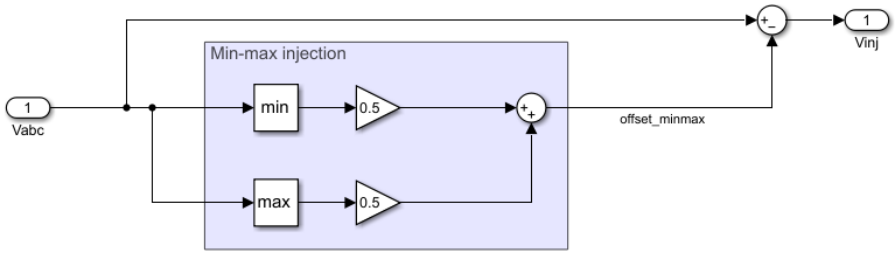

Figure 26: Third harmonic injection in the reference voltage signals obtained by the control.

4.2 Variable switching frequency control to reduce losses

For the validation of the variable switching frequency four speed points are analysed: $N_{mec} = 3000$rpm, $N_{mec} = 8000$rpm, $N_{mec} = 11000$rpm, $N_{mec} = 16000$ and $N_{mec} = 20000$rpm (see Figure 27). The first to analysed speed points are in the constant torque region whereas the last two are in the flux-weakening region. Figure 28 shows the corresponding switching frequency for each analysed speeds are 5kHz, 8.8kHz, 12.1kHz and 17.6kHz and 22kHz.

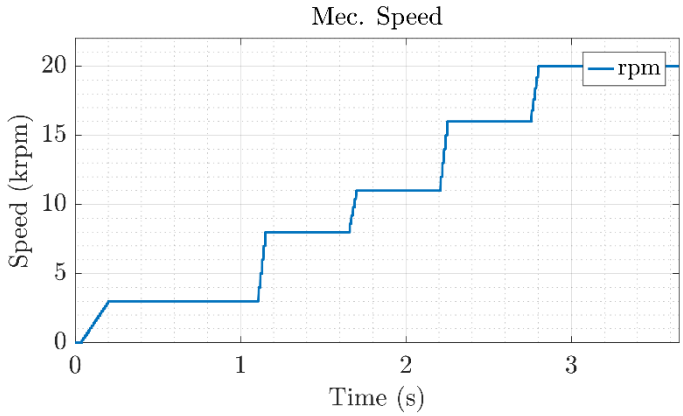

Figure 27: Mechanical speed profile for the variable switching control.

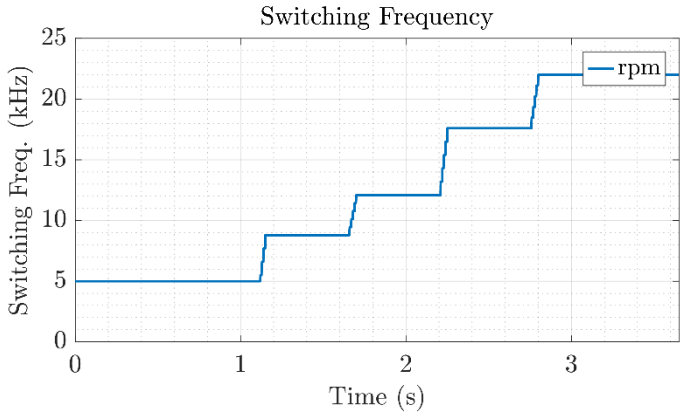

Figure 28: Selected switching frequency profile for the variable switching frequency control.

The resultant torque for the variable switching control is shown in Figure 29. In the two first analysed speed points $\Delta T_{em} = 5.42\%$ and $\Delta T_{em} = 14.31\%$. When $N_{mec} = 16000$rpm the resultant torque ripple is $\Delta T_{em} = 3.965\%$ and at the maximum speed ($N_{mec} = 20000$rpm), $\Delta T_{em} = 16.05\%$.

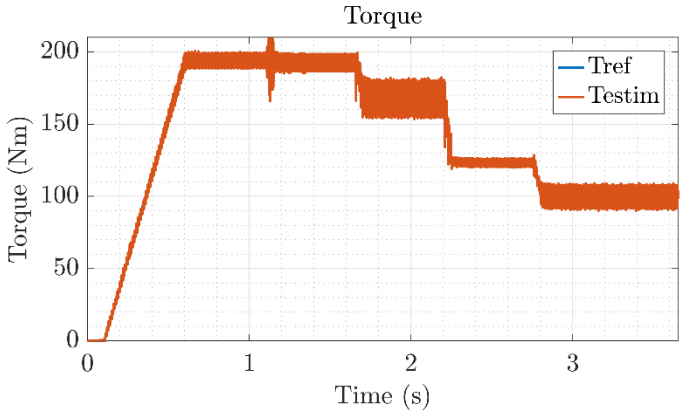

Figure 29: Reference and measured torque for the variable switching frequency control.

As for the previously presented control technique, the currents i_d and i_q are directly and indirectly proportional to the speed of the machine, respectively. In Figure 30 the resultant i_{dq} currents for the variable switching frequency control are shown. The resultant peak-to-peak i_{dq} currents for the analysed speed points are presented in Table 5.

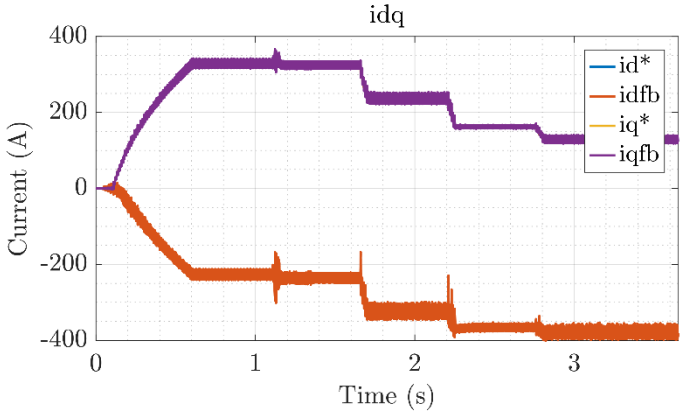

Figure 30: Reference and measured dq currents for the variable switching frequency control.

Table 5: Peak-to-peak curent values for idq currents

N_{mec}	$\lvert\Delta i_{d\ pp}\rvert$	$\lvert\Delta i_{q\ pp}\rvert$
3000 rpm	28.83 A	24.52 A
8000 rpm	25.2 A	19.05 A
11000 rpm	46.55 A	31.15 A
16000 rpm	21.41 A	9.49A
20000 rpm	43.62 A	21.18 A

The voltage values change drastically its value when the flux-weakening region is reached as expected. This can be seen in Figure 31 which shows the *dq* voltages and in Figure 32 which shows the voltage amplitude of the stator.

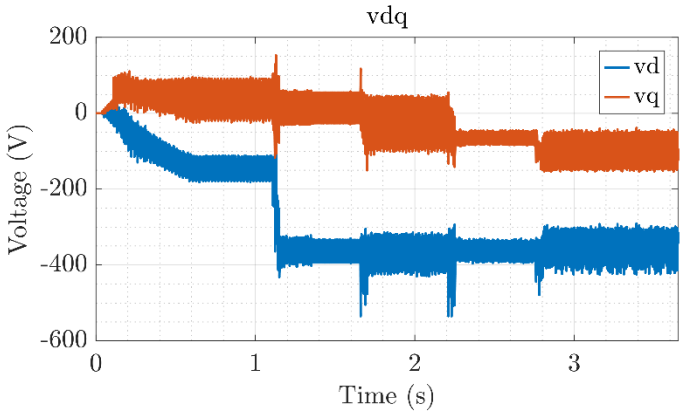

Figure 31: Reference and measured dq voltages for the variable switching frequency control.

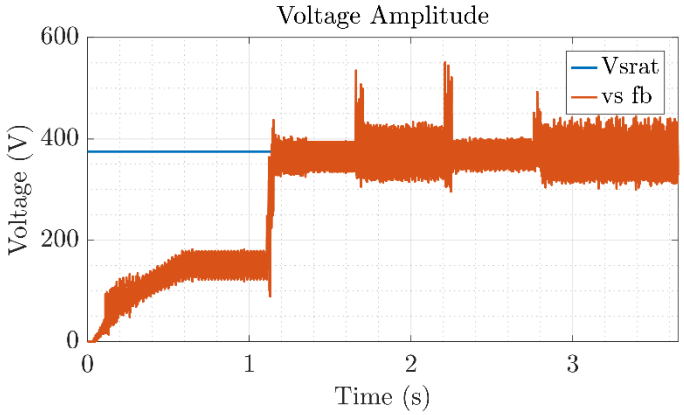

Figure 32: Rated voltage (blue) and voltage amplitude of the stator (red) for the variable switching frequency control.

In Figure 33 the resultant flux linkages in *dq* plane are shown. It can be noted that these fluxes have very similar current form as the *dq* currents. The reason for this is that the i_{dq} currents are dependent on the flux linkage. The flux amplitude of the stator is shown in Figure 34.

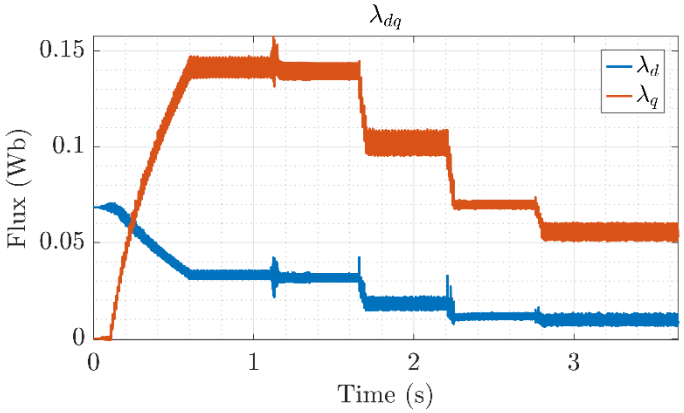

Figure 33: Flux in dq axes for the variable switching frequency control.

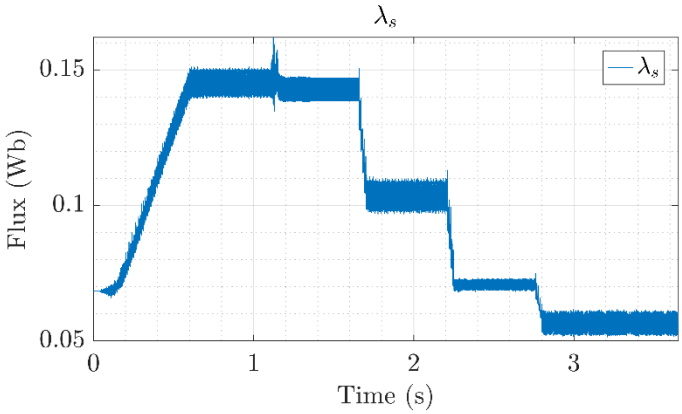

Figure 34: Flux amplitude of the stator for variable switching frequency control.

Finally, the phase currents of the machine are shown. The resultant phase current amplitude is shown in Figure 35.

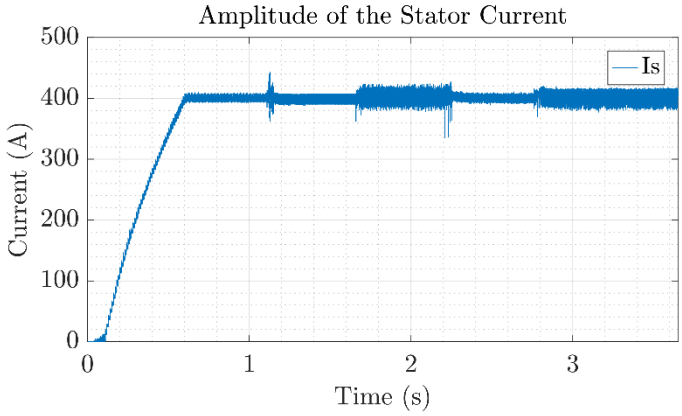

Figure 35: Phase current amplitude for the variable switching frequency.

In Figure 36, the zooms of the phase currents are shown. After the speed transitions, a sinusoidal phase current is maintained. The resultant THD for each analysed speed points are $THD_i = 2.77\%$, $THD_i = 2.37\%$, $THD_i = 1.39\%$ and $THD_i = 2.67\%$.

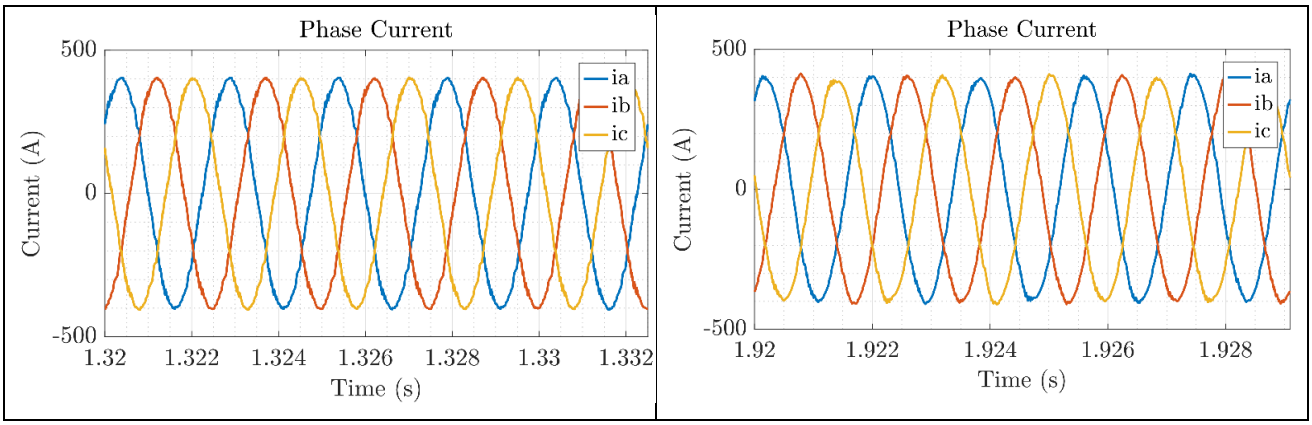

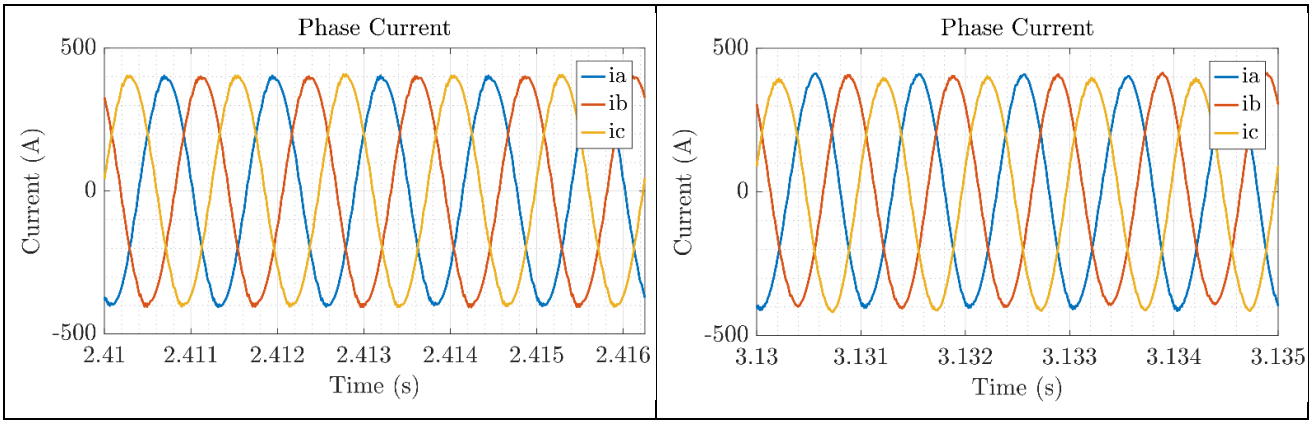

Figure 36: Zoom of the phase currents in the fours analysed speed points with the optimum switching frequency control. Respective speed points from left to right and from top to bottom: $N_{mec} = 8000rpm$, $N_{mec} = 11000rpm$, $N_{mec} = 16000rpm$ *and* $N_{mec} = 20000rpm$.

4.3 Optimal flux operation point to increase motor efficiency

In this section, the results in the full-speed range implementing the optimum flux control are shown. In Figure 37, the resultant torque results are shown when this control is applied. The shift between the constant torque region and the constant power region happens at $N_{mec} = 9285.71\text{rpm}$ and $t = 2.10\text{s}$. At this speed a torque value of 204Nm is achieved whereas at the maximum speed $T_{em} = 33.79\text{Nm}$. In Figure 38 the applied speed profile is shown, where the maximum speed is achieved at $t = 4.49\text{s}$.

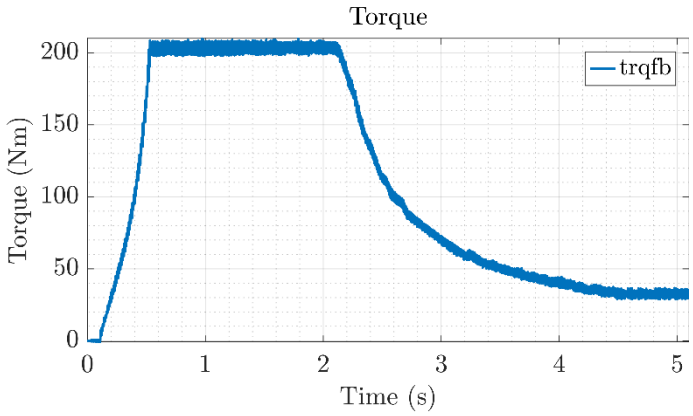

Figure 37: Torque simulation results with the optimum flux control.

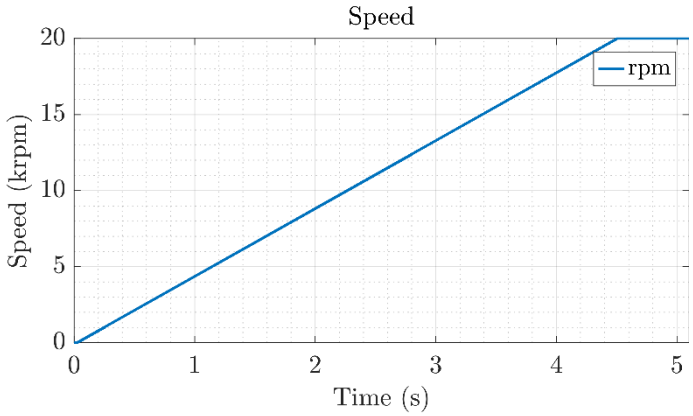

Figure 38: Applied speed profile with the optimum flux control.

The current references in dq coordinates and their respective measured feedback signals are shown in Figure 39. The PI current regulators, control correctly the currents when the optimum flux weakening region since the feedback signals track the calculated current references. After the flux weakening region is reached, the i_d current is reduced until -248.67A. The resultant amplitude of the stator current is shown in Figure 40. The reduction of the current amplitude yields to a power losses reduction which achieves a more efficient drive.

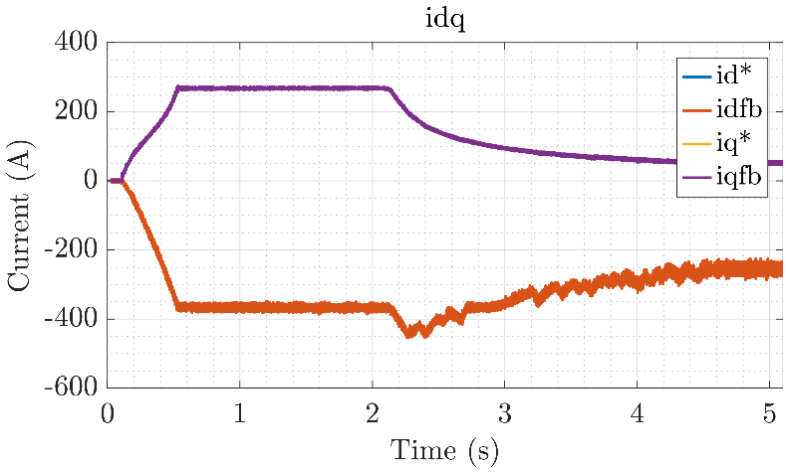

Figure 39: i_{dq} simulation results with the optimum flux control.

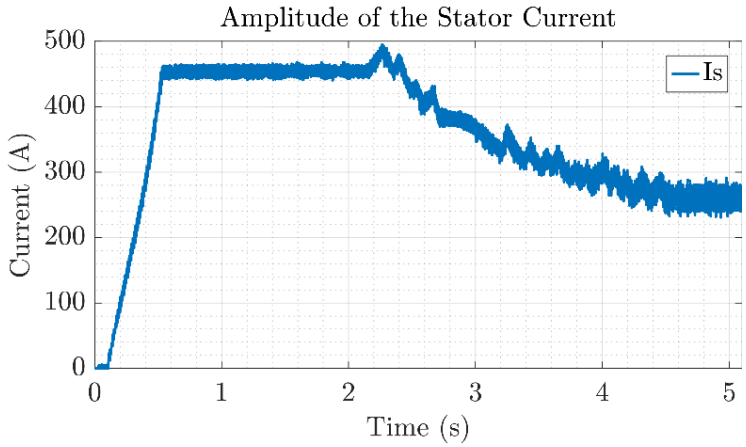

Figure 40: Amplitude of the stator current with the optimum flux control.

The phase currents in abc plane are shown in the next figures. The i_{abc} currents in the constant torque region are shown in Figure 41 where $\Delta i_{pk-pk} = 10.91$A is obtained with a current $THD_i = 1.55\%$. In Figure 42 the results for the flux weakening region are shown. The amplitude is reduced to $|I_a| = 266.91$A with a resultant $THD_i = 3.99\%$.

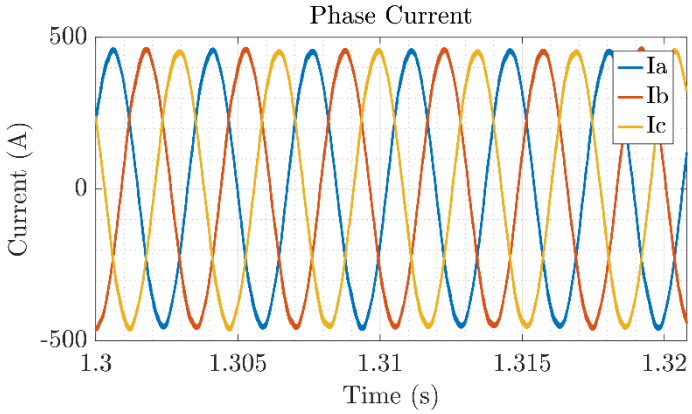

Figure 41: Phase currents in abc plane at the constant torque region with optimal flux control.

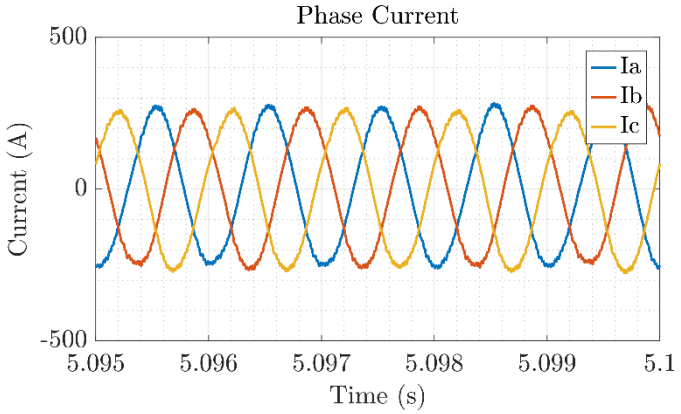

Figure 42: Phase currents in abc plane at the flux-weakening region with optimal flux control.

The resultant stator flux in dq planes are shown in Figure 43. In the constant torque region, the maximum achieved stator flux values are $\lambda_d = 11.98$mWb and $\lambda_q = 115.37$mWb. On the other hand, in the flux-weakening region, the minimum achieved stator flux values are $\lambda_d = 29.2$mWb and $\lambda_q = 22.48$mWb. In Figure 44, the amplitude of the stator flux is shown. In the constant torque region, a maximum stator flux $\lambda_s = 115.83$mWb whereas in the flux weakening region, the minimum achieved stator flux is $\lambda_s = 35.77$mWb.

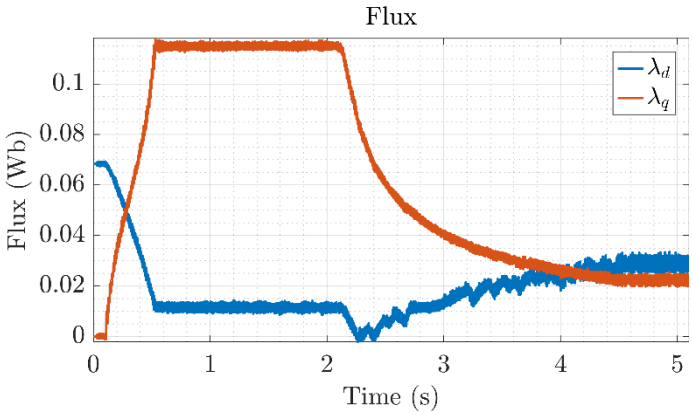

Figure 43: Stator flux in dq coordinates with optimum flux control.

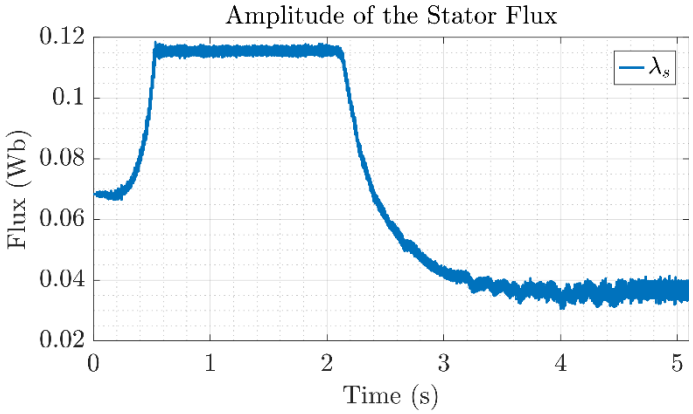

Figure 44: Stator flux amplitude with the optimum flux control.

The output of the PI current controllers is the v_{dq} voltages. These results are shown in Figure 45. At $N_{mec} = 9285.71$rpm, the amplitude of v_d voltage is reduced drastically, reducing at the same time the voltage amplitude of the stator. At the maximum speed, $v_s = 238.25$V is achieved. The resultant amplitude of the stator is shown in Figure 46.

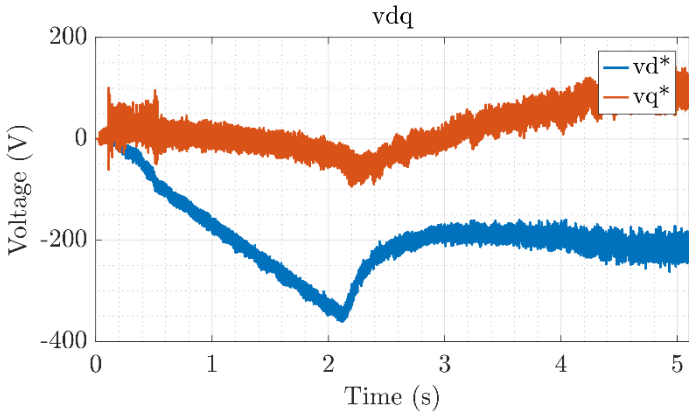

Figure 45: Stator voltage in dq coordinates with optimum flux control.

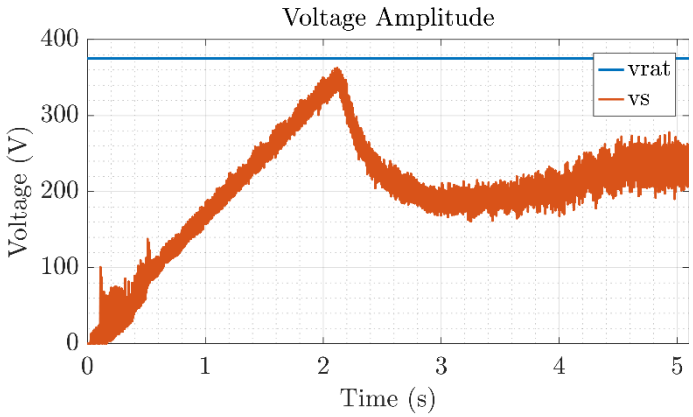

Figure 46: Voltage amplitude with the optimum flux control.

Since the amplitude of the voltage is reduced, the duty cycle follows the same pattern. The resultant maximum duty cycle is 0.976 whereas at the maximum speed, the resultant duty cycle is 0.86. The resultant duty cycle is shown in Figure 47.

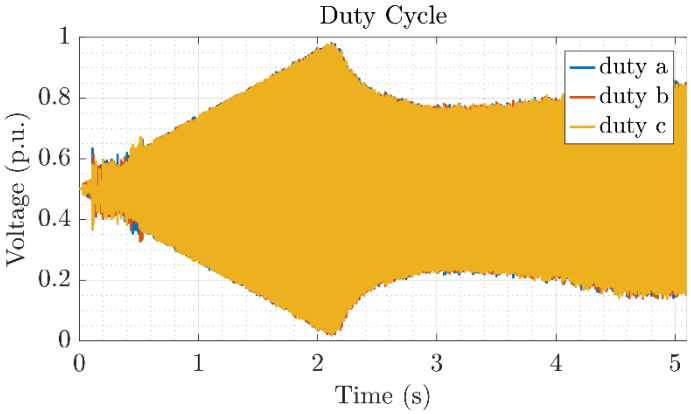

Figure 47: Duty cycle simulation results with optimum flux control.

4.4 Improved powertrain thermal management strategy

Based on motor or inverter high temperature a derating will be applied to reduce thermal stress in the drive. Thermal simulations are usually very long, in this case a very short simulation (5s) has been carried out to show how the algorithm should work. A hypothetical temperature profile is set, which can be seen in Figure 48. The applied speed profile is shown in Figure 49, which is the same as the one applied in the other analysed control strategies.

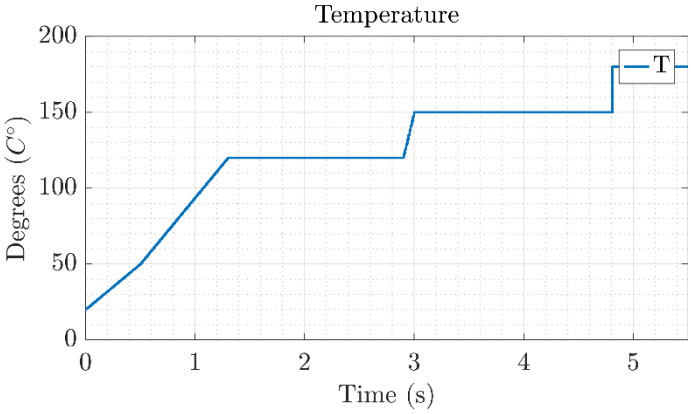

Figure 48: Applied temperature profile in the thermal management strategy control.

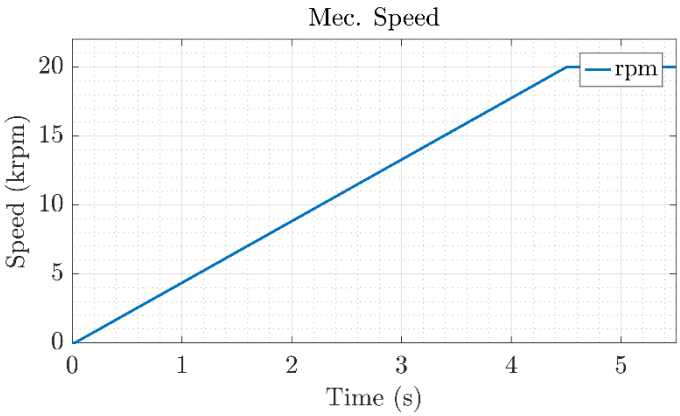

Figure 49: Applied speed profile in the thermal management strategy control.

When the temperature achieves 120℃ a derating of 0.75 is applied. The derating factor shown in Figure 50 is applied in function of the temperature shown in Figure 48.

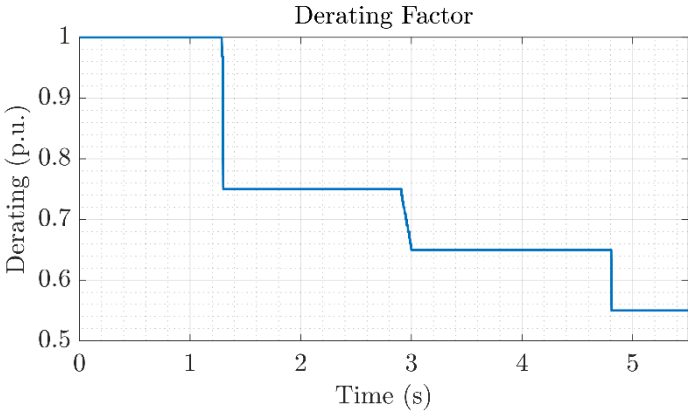

Figure 50: Applied derating factor for the thermal management strategy control.

In Figure 51, the reference and the measured i_{dq} currents are shown. The yellow and the blue lines are the current references without the thermal management strategy control. It can be seen how the derating factor shown in Figure 50 is applied when the temperature value achieves 120℃. The resultant amplitude of the stator current is shown in Figure 52. At the maximum speed a $THD_i = 5.71\%$ and an amplitude $I_s = 221.1$A Is obtained. With this strategy, the amplitude of the stator current is reduced reducing the thermal stress in the drive.

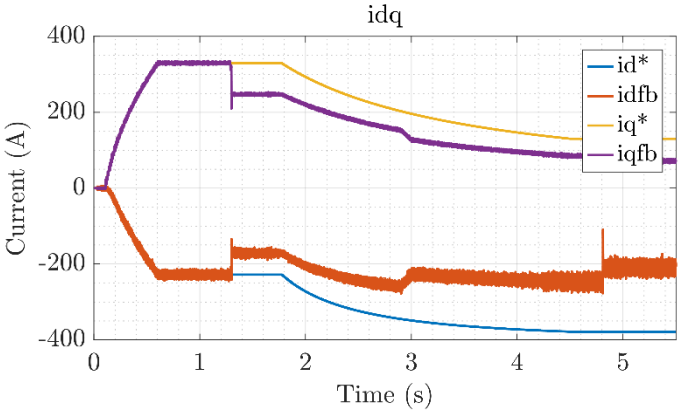

Figure 51: Currents in dq-plane for the thermal management strategy control.

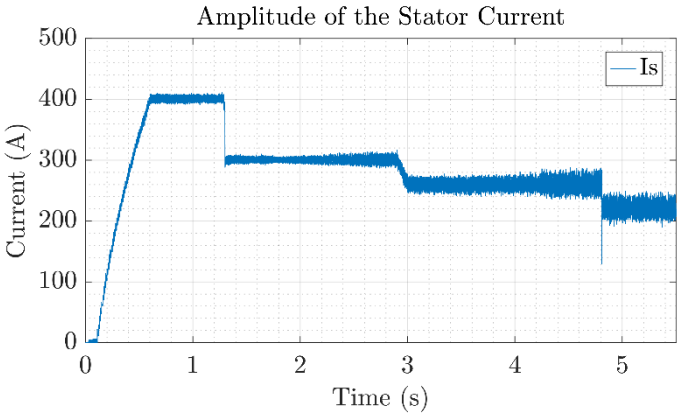

Figure 52: Amplitude of the stator current for the thermal management strategy control.

The resultant torque profile is shown in Figure 53. The blue line is the torque reference without the thermal management strategy control. The torque has the same behaviour as the i_{dq} currents, when the temperature achieves 120℃, the torque is reduced. After applying the derating due to the surpassing of the stablished temperature threshold, a torque ripple of $\Delta T_{em} = 4.82\%$ is obtained ($t = 1.35$s). At the maximum speed $\Delta T_{em} = 10.81\%$.

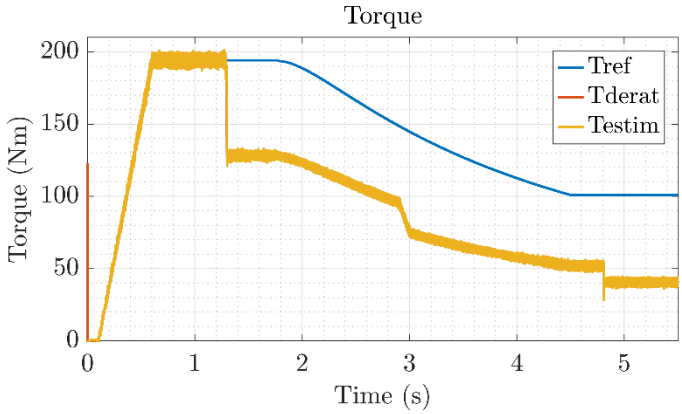

Figure 53: Resultant torque for the thermal management strategy control.

The resultant stator flux in dq- plane are shown in Figure 54 and the amplitude of the stator flux is shown in Figure 55. As expected, the amplitude of the stator flux is reduced as the temperature increases. In the constant torque region, the flux is reduced from $\lambda_s = 143\text{mWb}$ to $\lambda_s = 116\text{mWb}$.

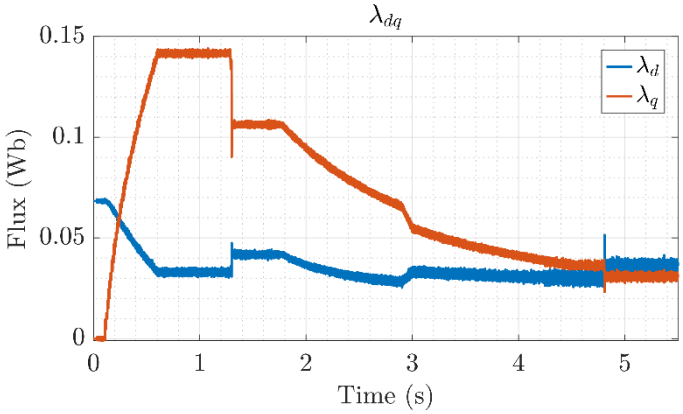

Figure 54: Stator flux in dq-plane for the thermal management strategy control.

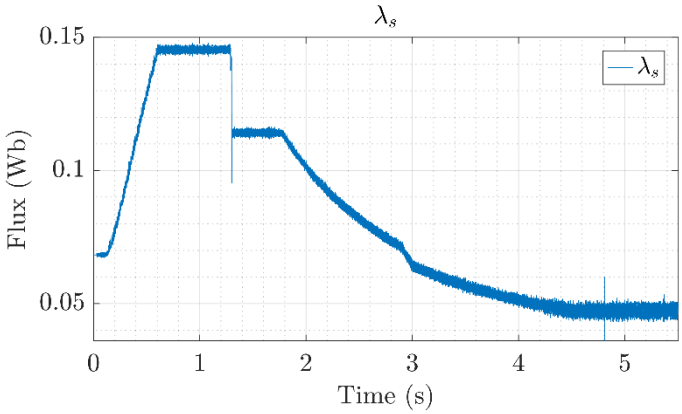

Figure 55: Amplitude of the stator flux for the thermal management strategy control.

Finally, the output voltages of the PI current regulators are shown in Figure 56. The amplitude of the voltages are increased due to the reduction in the stator flux after applying the derating due to the temperature constraint. The resultant stator voltage amplitude is shown in Figure 57. With this control strategy, the resultant voltage amplitude stator at the maximum speed is $V_s = 298.9\text{V}$.

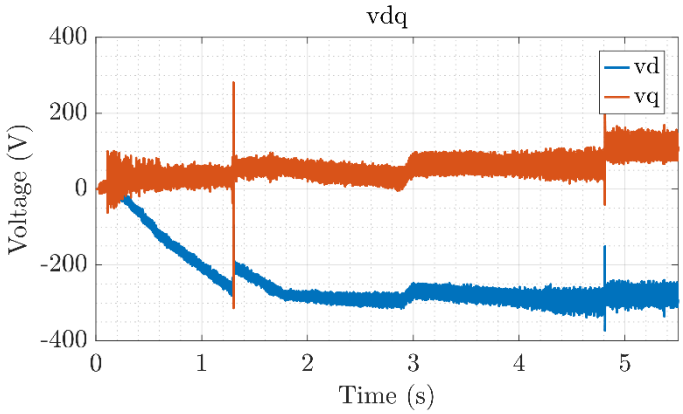

Figure 56: Voltages in dq-plane for thermal management strategy control.

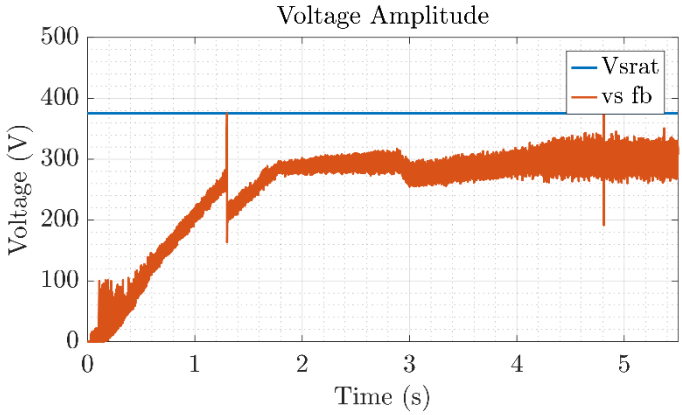

Figure 57: Amplitude of the stator voltage for the thermal management strategy control.

During the validation phase, in WP5, this improved powertrain thermal control strategy will be tunned based on inverter and motor experimental thermal data.

5 SIMULATIONS RESULTS: C+D+E SEGMENT MOTOR USE CASE

Even if the C+D+E segment motor design is not finished yet. Based on some preliminary design data (see Table 6), some simulation results are shown in this chapter to prove that the same control strategy is valid for both motors. Only the tunning of the control parameters should be modified.

Table 6 C+D+E segment motor design parameters (at maximum saturation levels).

C+D+E HEFT motor		
Pole pair	[-]	3
L_d	[mH]	0.192
L_q	[mH]	0.516
R_s	[mΩ]	36.3
Magnet flux (RMS)	[mWb]	94.2

The results in the full-speed range for the C+D+E segment motor user case. In Figure 58, the resultant torque results are shown when this control is applied. The shift between the constant torque region and the constant power region happens at $N_{mec} = 5357.1$rpm and $t = 1.22$s. At this speed a torque value of 340Nm is achieved whereas at the maximum speed $T_{em} = 127$Nm. The applied speed profile is shown in Figure 59, where the maximum speed is achieved at $t = 4.49$s.

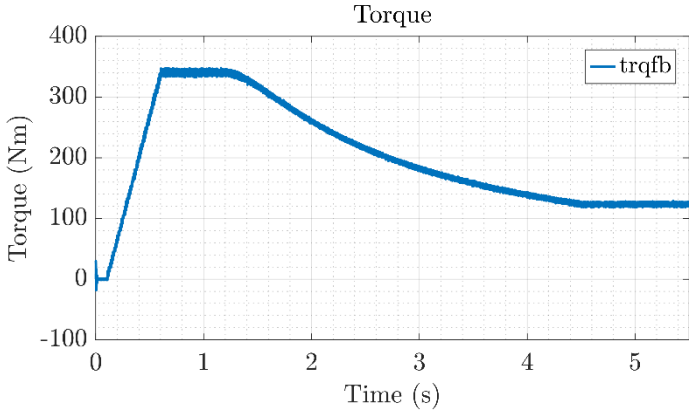

Figure 58: Resultant torque profile for Motor Segment C-D-E.

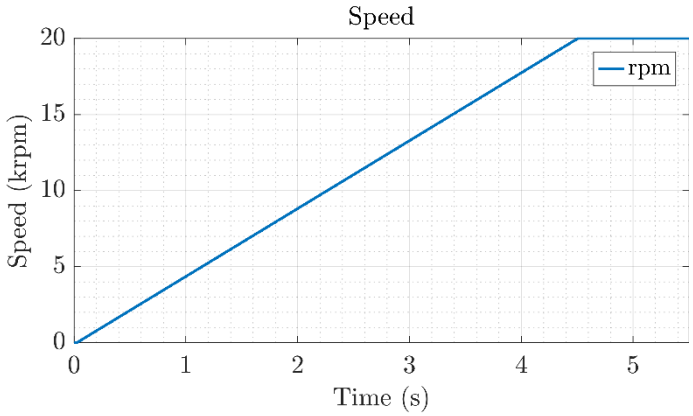

Figure 59: Applied speed profile for Motor Segment C-D-E.

In Figure 60 the current references in dq coordinates and their respective measured feedback signals are shown. The PI current regulators, control correctly the currents when the optimum flux weakening region since the feedback signals track the calculated current references. After the

flux weakening region is reached, the i_d current is increased until -474.64A. The resultant amplitude of the stator current is shown in Figure 61.

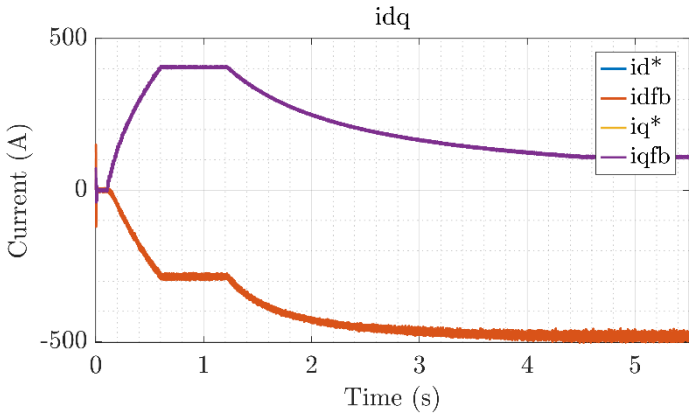

Figure 60: Reference and measured currents in dq plane for Motor Segment C-D-E.

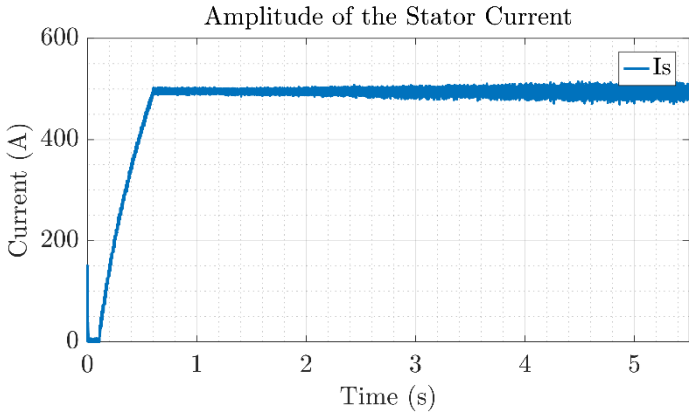

Figure 61: Amplitude of the stator current for Motor Segment C-D-E.

Five periods of the phase currents in abc plane are shown in Figure 62 and Figure 63 for constant torque region and flux-weakening region, respectively. In the constant torque region, $THD_i = 1.03\%$ is achieved whereas in the flux weakening region, $THD_i = 1.45\%$ is achieved.

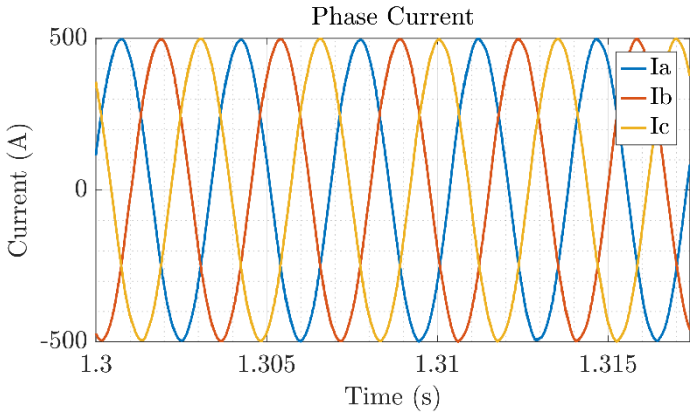

Figure 62: Phase current zoom in the torque constant region for Motor Segment C-D-E.

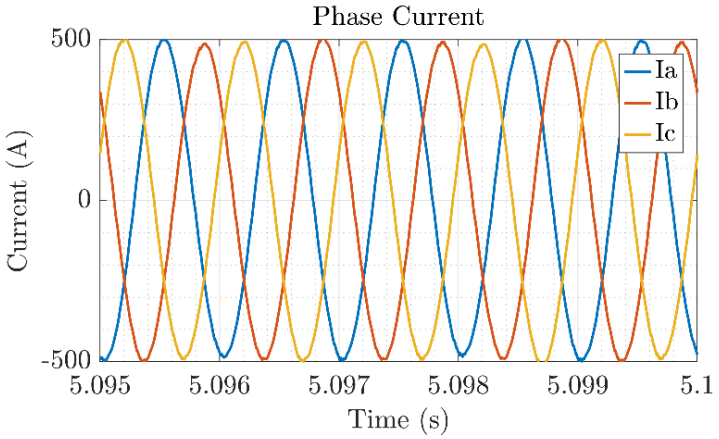

Figure 63: Phase current zoom in the flux-weakening region for Motor Segment C-D-E.

The resultant stator flux in dq planes are shown in Figure 64. In the constant torque region, the achieved stator flux values are $\lambda_d = 37.9$mWb and $\lambda_q = 209.08$mWb. On the other hand, in the flux-weakening region, the achieved stator flux values are $\lambda_d = 2.76$mWb and $\lambda_q = 74.58$. In Figure 65, the amplitude of the stator flux is shown. In the constant torque region, a maximum stator flux $\lambda_s = 212.63$mWb whereas in the flux weakening region, the minimum achieved stator flux is $\lambda_s = 58.4$mWb.

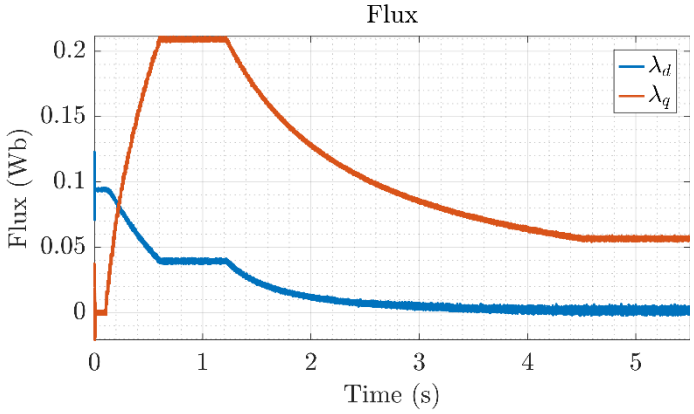

Figure 64: Stator flux in dq coordinates for Motor Segment C-D-E.

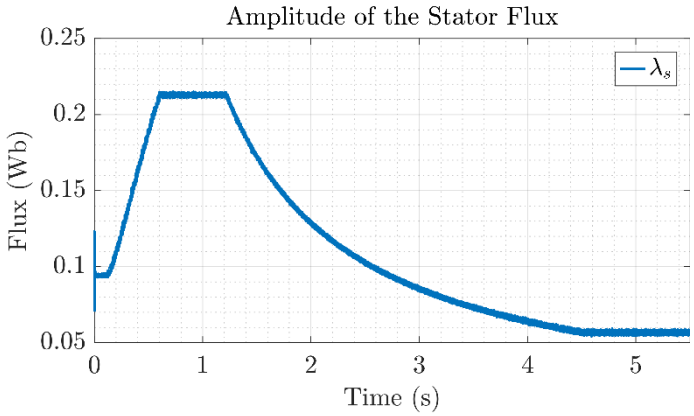

Figure 65: Stator flux amplitude for Motor Segment C-D-E.

The output of the PI current regulators is the v_{dq} voltages, which are shown in Figure 66. The resultant voltage amplitude is shown in Figure 67. As shown in this figure, the maximum voltage value is achieved at $t = 1.22$s, which correspond to the shift from constant torque region to the flux weakening region.

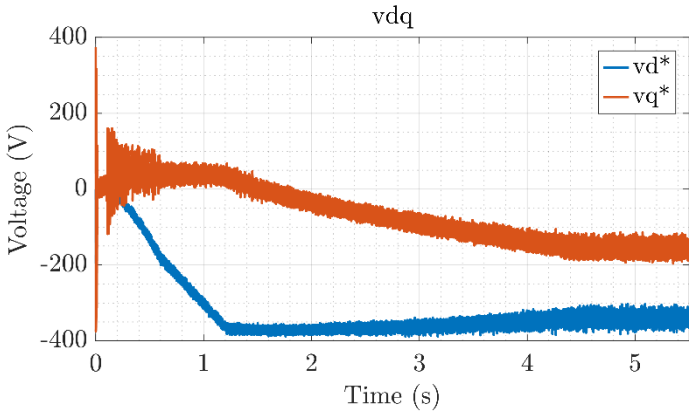

Figure 66: Stator voltage in dq coordinates for Motor Segment C-D-E.

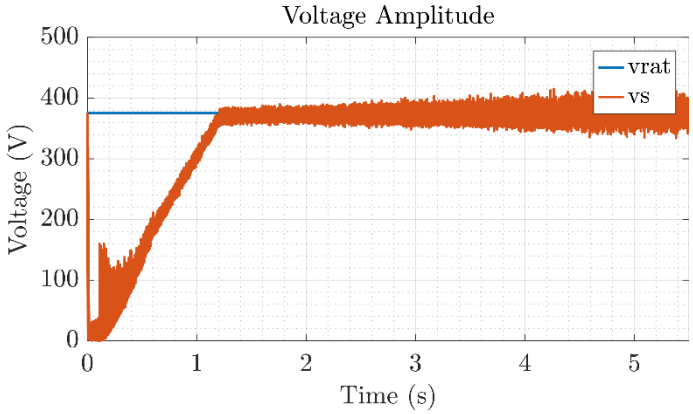

Figure 67: Stator voltage amplitudes for Motor Segment C-D-E.

6 DELIVERY DEVIATIONS FROM THE INITIAL PLANNING

There has been a delay in the delivery of D3.2. Improved SiC-based high voltage drive control.

Contractual delivery: 2024-05-31

Deliverable Date: 2024-07-04

This delay is due to a delay during C+D+E segment motor design. Some preliminary parameters were needed to carry out the tunning of the control strategy.

Administrative deviations:

First full version of this document (v1.0) has been uploaded to the TEAMS platform at the mid of February. Then, the document was shared between all WP3 partners to collect their comments and correction. After that, a new version was shared again to be reviewed by the coordinator.

Delay effect on overall project planning: This report is only related to WP3 and it does not have any impact in Task 3.3 which is running. So, it does not generate any delay in the project.

7 CONCLUSIONS

In this deliverable the work carried out in Task 3.2 of HEFT project has been summarized. The objective of this task was to improve SiC-based drive control to reduce powertrain losses and improve EV range. For that, firstly the IPMSM vector control has been explained. After that, online variable switching frequency control strategy to optimize drive operation has been implemented. Then, optimal flux operation point algorithm has been developed to increase motor efficiency. Finally, powertrain thermal management strategy has been developed.

All these control aspects will be used in both A+B segment motor and C+D+E segment motor, as control strategy is the same for both motors that will be designed in HEFT project (only some parameters' tunning need to be modified). Therefore, as use case, A+B segment motor has been selected, because this motor has already been designed. However, some preliminary results regarding C+D+E segment motor are also shown in this deliverable (this motor is still under development) to show that the proposed control strategy is valid for any IPMSM.

During the validation phase, in WP5, the improved powertrain thermal control strategy will be tunned based on inverter and motor experimental thermal data.

8 REFERENCES

[1] Abad G. et al “Power Electronics and Electric Drives for Traction Applications”, John Wiley & Sons, 2017, pp. 100-147. Print ISBN:9781118954423

[2] Oier Oñederra et al. “Three-Phase VSI Optimal Switching Loss Reduction Using Variable Switching Frequency”. In: IEEE Transactions on Power Electronics 32.8 (2017), pp. 6570–6576. doi: 10.1109/TPEL.2016.2616583.

[3] Dong Jiang and Fei Wang. “Variable Switching Frequency PWM for Three-Phase Converters Based on Current Ripple Prediction”. In: IEEE Transactions on Power Electronics 28.11 (2013), pp. 4951–4961. doi: 10.1109/TPEL. 2013.2240701.

[4] Kazuki Ohta et al. “Variable Switching Frequency Control for Efficiency Improvement of Motor Drive System by Using GaN Three Phase Inverter”. In: 2020 IEEE International Conference on Industrial Technology (ICIT). 2020, pp. 119–123. doi: 10.1109/ICIT45562.2020.9067266.